

Strong Coupling Constant Determination from the new CTEQ-TEA Global QCD Analysis

Alim Ablat,^{1,*} Sayipjamal Dulat,^{2,3,†} Marco Guzzi,^{4,‡} Joey Huston,^{3,§}

Kirtimaan Mohan,^{3,¶} Pavel Nadolsky,^{3,**} Dan Stump,^{3,††} and C.-P. Yuan^{3,‡‡}

¹*School of Physics and Electrical Engineering, Kashi University, Kashi, Xinjiang 844000 China*

²*School of Physics Science and Technology, Xinjiang University, Urumqi, Xinjiang 830046 China*

³*Department of Physics and Astronomy,*

Michigan State University, East Lansing, MI 48824, USA

⁴*Department of Physics, Kennesaw State University, Kennesaw, GA 30144, USA*

(Dated: March 18, 2026)

We present a new determination of the strong coupling constant α_s from a global QCD analysis CT25 of parton distribution functions (PDFs) that incorporates high-precision experimental measurements from the Run-2 of the Large Hadron Collider together with a large sample of other measurements over a wide interval of energies. This work addresses two objectives: providing an up-to-date determination of α_s using NNLO calculations and a sensitive nucleon data set within a self-consistent framework, and critically assessing the robustness of the $\alpha_s(M_Z)$ extraction in light of systematic uncertainties as well as correlations of $\alpha_s(M_Z)$ with the functional forms of PDFs and other model parameters. In regard to the uncertainty assessment, we demonstrate that some commonly used criteria, including the dynamical tolerance and Bayesian hierarchical models, may produce significantly different or even unstable estimates for the net α_s uncertainty, and we introduce a concept of *data-clustering safety* that the replicable uncertainty estimates must satisfy. Based on this in-depth examination of the CT25 global hadronic data set using a combination of analysis methods, and after demonstrating a weak correlation between α_s and the functional forms of CT25 PDF parametrizations, we find $\alpha_s(M_Z) = 0.1183^{+0.0023}_{-0.0020}$ at the 68% credibility level.

* alimjanablat@outlook.com

† sdulat@hotmail.com

‡ mguzzi@kennesaw.edu – Corresponding Author

§ huston@msu.edu

¶ kamohan@msu.edu – Corresponding Author

** nadolsky@msu.edu – Corresponding Author

†† stump@pa.msu.edu

‡‡ yuanch@msu.edu

CONTENTS

I. Introduction	3
II. Relevant aspects of the CT25 global analysis	6
II.1. Selection of data sets	6
II.2. The CTEQ-TEA goodness-of-fit function	10
II.3. Limitations of existing models for correlated systematics	11
III. Sources of uncertainties on QCD coupling	12
III.1. The PDF parametrization uncertainty is small...	12
III.2. ...but the systematic uncertainty remains	15
IV. Uncertainty estimation: tolerances	20
IV.1. The $\Delta\chi^2 = 1$ criterion	20
IV.2. The Particle Data Group prescription	21
IV.3. Global and Dynamical Tolerance Criteria	22
IV.4. Properties of the dynamic tolerance	24
IV.5. Data clustering safety of uncertainty estimates	27
IV.6. Data reclustering and K-folding	28
IV.6.1. Reclustering algorithm	29
IV.6.2. K-folding impact on α_s	29
V. Bayesian Models for Uncertainty Estimation	32
V.1. A Bayesian Hierarchical Model	32
V.2. A Gaussian Mixture Model	34
VI. Final combination of α_s determinations	35
VI.1. The central α_s value	36
VI.2. Final α_s determination	36
VII. Conclusions	37
Acknowledgments	39
A. New LHC data sets included in the CT25 NNLO analysis	40
B. Investigation of reclustering prescriptions	42

C. A toy example of uncertainty under K-folding	44
D. Information Criteria and the GMM	46
E. Sensitivity to charm-quark mass variations	48
References	49

I. INTRODUCTION

The strong coupling constant α_s is a fundamental parameter of the QCD Lagrangian that enters theoretical computations for all hadronic scattering processes. A precise and accurate determination of $\alpha_s(Q)$ and its dependence on the energy scale Q is of vital importance for the current precision-frontier program at the Large Hadron Collider (LHC), where vast amounts of data are being gathered and push the boundary of precision measurements to the next level [1]. The upcoming high-luminosity phase of the LHC (HL-LHC) will further increase the volume of high-precision data, demanding a matching increase in both the detector capabilities and precision of theoretical calculations to properly validate relationships between fundamental parameters of the Standard Model (SM), constrain properties of the Higgs boson, and search for new physics. For instance, the running of α_s at the highest achieved energies may reveal the presence of new colored particles and influence the scale at which the SM couplings may unify. Variations in the observed $\alpha_s(M_Z)$ at the scales of order of the Z boson mass, M_Z , can affect projections for the range of energies at which the electroweak (EW) vacuum might shift from a metastable to a stable configuration.

Hence, the QCD coupling and its estimated uncertainty play a pivotal dual role of characterizing the universal force of nature and, at the same time, serving as a precise theoretical input for many standard candle processes in ongoing experiments. In particular, top-quark pair and Higgs boson production cross sections are very sensitive to the assumed $\alpha_s(M_Z)$. The associated uncertainty, which is correlated in hadron-collider predictions with the PDF uncertainty, can potentially exceed those due to the scale dependence and experimental errors [2, 3].

The Particle Data Group (PDG) currently reports the uncertainty on $\alpha_s(M_Z)$ of about 0.8%, resulting in a value of $\alpha_s(M_Z) = 0.118 \pm 0.0009$ [4]. This result is derived from a compilation of lattice and non-lattice results, which independently provide compatible central values of $\alpha_s(M_Z)$ and of its uncertainty. The corresponding relative uncertainty exceeds that achieved for the fundamental couplings of electroweak and gravitational interactions. The new twist is that the latest determinations of α_s from high-statistics experimental measurements and lattice QCD may individually quote a comparable and — perhaps in

the future — a smaller uncertainty than the PDG world-average uncertainty of ± 0.0009 . Along these lines, the ATLAS collaboration measured $\alpha_s(M_Z) = 0.1183 \pm 0.0009$ [5] using data of Z boson transverse-momentum distributions at $\sqrt{s} = 8$ TeV. The CMS collaboration simultaneously extracted $\alpha_s(M_Z)$ and PDFs [6] from a global QCD analysis at NNLO using double-differential cross section measurements of inclusive jet production at $\sqrt{s} = 2.76, 7, 8,$ and 13 TeV combined with deep inelastic scattering (DIS) data from HERA. They obtained $\alpha_s(M_Z) = 0.1176^{+0.0014}_{-0.0016}$. Other recent relevant α_s determinations from the CMS and ATLAS collaborations can be found in Refs. [5, 7–9]. Several determinations from deep inelastic scattering (DIS) at ep collider HERA find a somewhat lower α_s value than at the LHC, such as $\alpha_s(M_Z) = 0.1142 \pm 0.0028$ determined by H1 collaboration in a simultaneous fit of α_s and proton PDFs [10]. Independently, lattice QCD determines α_s from several types of nonperturbative computations. The Flavor Lattice Averaging Group (FLAG) systematizes and cross-validates these determinations. It recently reports $\alpha_s(M_Z) = 0.1183 \pm 0.0007$ [11].

The studies of α_s thus enter a new phase when its precision may eventually be pushed to 0.1% across diverse observations in the next two decades [1], while in the meantime novel challenges will need to be confronted in both the individual α_s measurements and their combination. It is expected that, at this precision level, the growing complexity of involved systematic factors raises the chance for misestimations. When the misestimations go unnoticed – an unwanted but common occurrence encountered in complex studies across many disciplines [12] – the uncertainty tends to be underestimated; some measurements of the parameter are not replicated by its independent determinations. When replicability degrades, a PDG or another combination may need to inflate the stated uncertainties of measurements in order to make them statistically compatible. As an illustration, the Committee on Data of the International Science Council inflates the errors of highly precise measurements of Newton’s gravitational constant G by a factor of 3.9 in order to meaningfully combine them [13]. Within its small span, the combined uncertainty band on G does not overlap significantly with those of several most precise measurements, meaning it does not replicate them. This indicates a general trend that the measurements of fundamental constants eventually experience the tradeoff between the precision and replicability, when raising the former depletes the confidence in the latter. How far can the precision measurements of α_s go while remaining replicable? What can be done to control the uncertainty estimates and postpone the onset of non-replicability?

This article will critically explore these questions in the context of the precision determination of the $\alpha_s(M_Z)$ from the new CTEQ Tung Et Al. (CTEQ-TEA) global QCD analysis of nucleon scattering data, named “CT25” [14]. The primary goal of the global QCD analysis is to determine parametrizations of parton distribution functions (PDFs), as well as α_s and other QCD parameters, from a simultaneous fit

of a large, diverse collection of experimental measurements. The methodology of the global analysis offers the most complete view of the *correlated* constraints on α_s , heavy-quark masses, and the PDFs arising from a variety of scattering experiments with different systematic errors, with *simultaneous* dependence on all of them. This completeness gives the global analysis an edge over the standalone α_s determinations from the nucleon data, which typically neglect at least some of the correlation with the PDFs or other experiments. As such, and given the growing dominance of hadron scattering processes in experimental α_s determinations, the global analysis of PDFs is well suited for tests of uncertainty quantification and replicability in the α_s studies. Many combined analyses of the PDFs and α_s have been performed by our CTEQ-TEA group [15, 16] and other groups [17–22] over the years. The strong coupling α_s has recently been extracted from global QCD analyses, employing an approximate PDF evolution at the next-to-next-to-next-to-leading order (aN³LO) [23] in QCD by the MSHT group, and from an analysis using an aN³LO QCD evolution combined with the photon PDF at the next-to-leading order (NLO) in QED [24] by the NNPDF collaboration.

The CT25 global analysis determines α_s at the next-to-next-to-leading order (NNLO) in QCD by employing an improved methodology as well as an extended global data set in which precision LHC Run-2 measurements with high integrated luminosity augment those included in the CT18 study [16]. The novel feature of our study is that we determine the central value and uncertainty of α_s by several methods to obviate the dependence on the correlation with PDFs, selection of experiments, and systematic uncertainties in the experiments.

We do not resort to a single prescribed definition of the global PDF uncertainty (tolerance [25]) to estimate the allowed α_s range, in contrast to the previous combined PDF+ α_s fits. Instead, we determine the span of the α_s values consistent with the global data set at NNLO in several ways: (i) by generating the $\chi^2(\alpha_s)$ profile from a single fit, (ii) by comparing the α_s values from many fits with independent PDF parametrizations, and (iii) by combining the constraints from individual experiments according to several criteria to assess the uncertainty. The final α_s result is obtained by combining several such extractions.

The rest of this manuscript is organized as follows. In Sec. II, we briefly describe the methodology and advancements in the CT25 global PDF analysis. We summarize the new data sets included in the CT25 baseline, the definition of the figure-of-merit function χ^2 , and the implementation of correlated systematic errors provided by the experiments. Section III.1 explores the impact of the choice of PDF parametrizations on the α_s determination. We also review how $\alpha_s(M_Z)$ can be determined from the χ^2 scan over $\alpha_s(M_Z)$, and which criteria are applicable to determine the $\alpha_s(M_Z)$ error with this methodology.

Sec. III.2 critically examines the impact of the implementation of experimental systematic uncertainties on the extracted value of $\alpha_s(M_Z)$, and it discusses the handling of some observed disagreements

among data sets in the baseline. Section IV is dedicated to the exploration of uncertainty prescriptions (tolerances) according to the commonly used global and dynamical implementations. For the latter definition, we examine how the user-specified clustering of published data sets modifies the quantitative error estimates. We point out that either the dynamical tolerance in the Hessian method or K -folding in the Monte-Carlo method may produce uncertainties that depend on the user-chosen clustering of data sets. We introduce the concept of data clustering safety that must be addressed in such situations.

Sec. V describes Bayesian statistical models utilized for the combination of the results for $\alpha_s(M_Z)$ and its uncertainties, while Sec. VI obtains and compares the uncertainties using a variety of methods. This Section quotes our final α_s estimate. Sec. VII contains our conclusions. Technical details of several discussions are relegated to five Appendices. The default scale M_Z is to be assumed when the scale of α_s is omitted.

II. RELEVANT ASPECTS OF THE CT25 GLOBAL ANALYSIS

II.1. Selection of data sets

As in many general-purpose CTEQ-TEA fits, the CT25 NNLO global analysis has taken place over several years and now culminates with the release of the official CT25 PDF ensembles that update the previous generation of the PDFs [16] consisting of the default CT18 NNLO error set and three alternative, yet equally acceptable PDF ensembles, CT18Z, A, and X. A significant part of this effort went into an exploration of a large number of new candidate measurements for the extension of the CT18 baseline data set, focusing primarily on high-precision production of lepton pairs, hadronic jets, and top quark-antiquark pairs in the LHC Runs 1 and 2. We have documented these preliminary explorations in three publications [26–28]. Based on these studies, we selected a number of precise and mutually consistent data sets that are included in the final CT25 release. Several data sets included in CT18 have been updated or removed in the final CT25 fit, for the reasons that will be explained in the text.

The newly added LHC data sets in CT25 are listed in the upper part of Table I and reviewed in Appendix A. As its data baseline, CT25 started with the CT18A [16] global data set, which already included a combination of measurements in deep-inelastic scattering and production of lepton pairs, hadronic jets, and top-quark pairs at both fixed-target and collider energies. Notably, the CT18A baseline included a precision data set on W and Z production in the ATLAS experiment at 7 TeV [29], which offered the first evidence for the enhanced strangeness PDF at $x \approx 0.02$, in some disagreement with charged-current DIS experiments. More recent LHC measurements included in the CT25 fit are consistent with this strangeness enhancement, albeit with somewhat reduced magnitude.

The inclusion of the new LHC measurements, added on top of the CT18A baseline *without replacing or discarding any of the previously fitted experiments*, increased the number of data points, N_{pt} , by 769, the majority of which were from inclusive jet production and Drell-Yan triple-differential Z -boson production at ATLAS, cf. Table I. This version of the CT25 fit, which we will call “CT25prel”, has the largest $N_{\text{pt}} = 4450$ among the various CT25 candidate fits. This data set is not unique, however: other well-motivated data combinations are possible, as was also the case for CT18. When all data sets are retained in the CT25 baseline, we observe a reasonable, although not ideal, agreement among the global data, with significant pulls on the PDFs from the newly-fitted data. The most precise new experiments in the CT25 fits tend to exhibit an increase in χ^2/N_{pt} in a pattern similar to that observed in the CT18 global analysis. The new Drell-Yan and $t\bar{t}$ production data consistently prefer a softer gluon at intermediate-to-large x ($0.05 \leq x \leq 0.7$), while inclusive jet production data pull the gluon in the opposite direction in the large- x range. Overall, the cumulative effect of these measurements, when they are combined, amount to having a softer gluon at intermediate-to-large x , as compared to CT18A.

To investigate the range of valid PDF solutions in this new setting, we explored other related, also acceptable, branches of the CT25prel fit. The alternative choices made in these fits reflect the complexities present within the global fitting framework, many of which were highlighted in the preceding CT18 publication [16], as well as in a review [25].¹ In the end, we obtained the default CT25 fit, or just “CT25”, as follows. Compared to CT18A and CT25prel, we replaced the H1 measurements of charm and bottom semi-inclusive structure functions [30, 31] by their HERA combination [32], which moderately increased the corresponding χ^2 without substantially modifying the PDFs. We added the E906/SeaQuest measurement of the $\sigma_{pd}/(2\sigma_{pp})$ ratio in fixed-target Drell-Yan pair production [33]. We removed four data sets (336 points) on inclusive charged-current DIS on an iron target from the CDHSW [34] and CCFR [35, 36] collaborations, as they are in some tension with each other and increase dependence of CT25 results on the nuclear modifications of proton PDFs.² The weakly sensitive determination of the longitudinal structure function $F_L(x_B, Q^2)$ by the H1 collaboration [38] was also omitted without a noticeable impact on the PDFs. Finally, we replaced the CMS jet production datasets at 7, 8, and 13 TeV by their updated versions [6] that incorporate improved evaluations of systematic uncertainties and include statistical correlation matrices.

Turning back to Table I, the last column in its upper portion reports the χ^2/N_{pt} values for each experiment using the PDFs from the default CT25 NNLO and from the CT18A NNLO global fits (with the latter in parentheses). The errors express the corresponding asymmetric PDF uncertainties that

¹ In the context of CT18, we opted to publish four PDF ensembles to quantify some of these possibilities.

² The default CT25 fit nevertheless retains CCFR and NuTeV data sets on dimuon production in CC DIS on the isoscalar target, as those provide unique constraints on the strangeness PDF at $x > 0.05$. In both CT18 and CT25 fits, we apply a correction from [37] to approximate nuclear modifications in such experiments.

TABLE I. The upper part of the table lists the newly added data sets in the CT25 analysis, contributed by measurements of lepton-pair, top-quark-pair, and single-inclusive jet production from the LHC Runs 1 and 2. For these experiments, we report the χ^2/N_{pt} for the default CT25 and prior CT18A PDF ensembles, assuming $\alpha_s(M_Z) = 0.118$. Section II.2 provides the definition of χ^2 . The errors are asymmetric PDF uncertainties computed using a master formula in Ref. [39] and the error PDFs defined at 68% CL, according to the two-tier PDF tolerance employed in CT18. The lower part of the table shows the total numbers of points, χ^2/N_{pt} , and approximate preferred α_s in the default and preliminary CT25 fits described in the text, as well as in the CT18A fit.

New and updated LHC data sets in the CT25 NNLO analysis			
ID	Experiment	N_{pt}	χ^2/N_{pt} for $\alpha_s(M_Z) = 0.118$, CT25 (CT18A)
Lepton pair production			
211	ATLAS 8 TeV W [40]	22	$2.04^{+0.65}_{-0.52}$ ($4.35^{+2.65}_{-2.37}$)
212	CMS 13 TeV Z [41]	12	$2.02^{+1.03}_{-1.23}$ ($2.12^{+3.77}_{-0.17}$)
214	ATLAS 8 TeV Z 3D [42]	188	$1.16^{+0.14}_{-0.06}$ ($1.22^{+0.34}_{-0.14}$)
215	ATLAS 5.02 TeV W, Z [43]	27	$0.62^{+0.10}_{-0.09}$ ($0.77^{+0.34}_{-0.09}$)
217	LHCb 8 TeV W [44]	14	$1.39^{+0.34}_{-0.23}$ ($1.52^{+0.49}_{-0.36}$)
218	LHCb 13 TeV Z [45]	16	$1.09^{+0.49}_{-0.39}$ ($1.24^{+1.03}_{-0.38}$)
Inclusive jet production			
553	ATLAS 8 TeV jets [46]	171	$1.60^{+0.10}_{-0.06}$ ($1.57^{+0.12}_{-0.07}$)
554	ATLAS 13 TeV jets [47]	177	$1.32^{+0.06}_{-0.05}$ ($1.26^{+0.09}_{-0.03}$)
555	CMS 13 TeV jets [6, 48]	78	$1.13^{+0.11}_{-0.04}$ ($1.29^{+0.23}_{-0.17}$)
556	CMS 7 TeV jets [6, 49–51]	118	$0.74^{+0.02}_{-0.03}$ ($0.7^{+0.12}_{-0.03}$)
557	CMS 8 TeV jets [6, 52]	164	$1.17^{+0.12}_{-0.06}$ ($1.16^{+0.18}_{-0.06}$)
$t\bar{t}$ production at 13 TeV			
521	ATLAS all-hadronic $y_{t\bar{t}}$ [53]	12	$1.11^{+0.07}_{-0.07}$ ($1.06^{+0.10}_{-0.07}$)
528	CMS dilepton $y_{t\bar{t}}$ [54]	10	$1.28^{+0.43}_{-0.44}$ ($1.04^{+0.78}_{-0.44}$)
581	CMS lepton+jet $m_{t\bar{t}}$ [55]	15	$1.13^{+0.33}_{-0.31}$ ($1.36^{+0.89}_{-0.48}$)
587	ATLAS lepton+jet $m_{t\bar{t}} + y_{t\bar{t}} + y_{t\bar{t}}^B + H_T^{t\bar{t}}$ [56]	34	$1.07^{+0.19}_{-0.13}$ ($0.94^{+0.24}_{-0.10}$)
All experiments			
PDF ensemble	N_{pt}	χ^2/N_{pt} for $\alpha_s(M_Z) = 0.118$	Preferred $\alpha_s(M_Z)$
CT25 NNLO, with default data set [14]	4066	1.20 ± 0.009	≈ 0.1185
CT25prel, with augmented CT18A data set	4450	1.20 ± 0.010	≈ 0.1177
CT18A NNLO [16]	3674	1.19 ± 0.013	≈ 0.1165

are evaluated at the 68% credibility level (CL).³ Fitting the new experiments in the CT25 framework generally improves their χ^2 .

The lower portion of Table I compares the total numbers of points and χ^2/N_{pt} for the default CT25, CT25prel, and their CT18A predecessor. The last column of the lower part also shows the *approximate* preferred value of α_s in these three fits, which is further adjusted by modifications discussed in the rest of the article.

Upon the addition of the LHC data sets in CT25prel, the reference α_s increased from a range 0.1164–0.1169 in the CT18 series to ≈ 0.118 . To a large extent, this change is due to the preference for a softer gluon at the intermediate-to-large x , which is compensated by some increase in α_s .

In the default CT25 fit, the reference α_s is further increased to ≈ 0.1185 primarily because of the removal of the CDHSW inclusive charged-current DIS data set [34] on iron. The exclusion of the counterpart CCFR measurement had no appreciable effect, as it is known to be largely consistent with $\alpha_s(M_Z) \approx 0.118$ [57–60]. In the CT18 publication, we emphasized that the CDHSW data set is generally fitted well, yet its Q dependence differs from that of an analogous CCFR observation [61, 62].

The Lagrange Multiplier scans in the context of CT18 (see its Fig. 21 in Ref. [16]) indicated that CDHSW prefers a far larger gluon $g(x, Q)$ at $x > 0.1$ than the other experiments. This preference, in turn, suppresses the preferred α_s . For this reason, the two CDHSW data sets were included in CT18/CT18A/CT18X, but not in CT18Z. Aside from the impact on the fitted value of α_s , the removal of the inclusive neutrino-iron DIS data sets from the CT25prel PDF fit slightly (well within PDF uncertainties) reduced g and increased u and d PDFs at $x > 0.1$. Overall, these CDHSW and CCFR experiments do not manifestly disagree with the rest of the data.

Our general observation is then that the described revisions in the CT25 data set, as compared to the CT18A data set, tend to elevate the preferred α_s to above 0.118 *for the default settings of the global fit*. We further emphasize that this trend may change considerably under reasonable modifications in the fit’s settings, reflecting in part *inconsistencies (tensions) among the input data sets*, and in part the *modeling of experimental and theoretical systematic uncertainties*.

Many CPU-intensive studies were carried out with the CT25prel data set, and were not repeated for the (slightly different) CT25 data set. In the rest of this article, we will present studies with either CT25prel or with CT25, without loss of generality.

³ The PDF fits base themselves on the Bayesian paradigm, and hence the interpretation of their errors on the PDFs and α_s as “credibility intervals” is appropriate. That said, these errors are also used to predict the frequency of future measurements using the determined parameters, in which case the users may view them as “confidence intervals”.

II.2. The CTEQ-TEA goodness-of-fit function

In the exploration of uncertainties, we will repeatedly turn to the goodness-of-fit (GOF) function $\chi^2 \equiv -2 \ln P(T|D)$, minimized with respect to all free parameters in the fit to maximize the posterior probability $P(T|D)$. The CT25 analysis implements it as

$$\chi^2 = \chi_R^2 + \chi_{\text{LM}}^2, \quad (2.1)$$

where χ_R^2 quantifies the agreement of theory with experiments, and χ_{LM}^2 is a generally small contribution imposing theoretical priors on the PDFs. The latter is constructed from Lagrange-Multiplier (LM) contributions whose role is to (i) enforce physical behavior of PDF flavor ratios in the extrapolation regions with poor constraints from the data and (ii) enable a ‘‘ridge’’ (L2) regularization on a few poorly constrained, yet correlated free parameters.

In a fit with N_E data sets, the first term in Eq. (2.1),

$$\chi_R^2 \equiv \sum_{E=1}^{N_E} \chi_E^2, \quad (2.2)$$

is a sum of contributions χ_E^2 from individual data sets E given by [16, 39]

$$\begin{aligned} \chi_E^2(\mathbf{a}, \boldsymbol{\lambda}, \alpha_s, \{m_q\}) = \\ \sum_{k=1}^{N_{\text{pt}}^{(E)}} \frac{1}{s_k^2} \left(D_k - T_k(\mathbf{a}, \alpha_s, \{m_q\}) - \sum_{\alpha=1}^{N_\lambda^{(E)}} \beta_{k\alpha}(\mathbf{a}, \alpha_s, m_q) \lambda_\alpha \right)^2 + \sum_{\alpha=1}^{N_\lambda^{(E)}} \lambda_\alpha^2. \end{aligned} \quad (2.3)$$

Here D_k and T_k are the k -th central experimental and theory values, respectively, $s_k = \sqrt{s_{k,\text{stat}}^2 + s_{k,\text{uncor sys}}^2}$ is the total uncorrelated error on the measurement D_k , and $\beta_{k\alpha}^{(E)}$ is the correlation matrix of systematic uncertainties. $\mathbf{a} \equiv \{a_1, a_2, \dots, a_{N_{\text{pdf}}}\}$ and $\boldsymbol{\lambda} \equiv \{\lambda_1, \dots, \lambda_{N_\lambda^{(E)}}\}$ are the vectors of PDF parameters and systematic nuisance parameters of E , with the latter commonly assumed to be random and distributed according to the standard normal distribution $\mathcal{N}(0, 1)$. Equation (2.3) indicates that χ^2 generally depends on QCD parameters – α_s and quark masses m_q – both through the theoretical predictions T and the experimental correlation matrices $\beta_{k\alpha}$, although this dependence of the latter is usually neglected.

In our study, we minimize the total χ^2 with respect to α_s and \mathbf{a} , while using constant $\{m_q\}$ and profiling [63] the nuisance parameters $\boldsymbol{\lambda}$ for every $\{\alpha_s, \mathbf{a}\}$ combination. We will find it helpful that, at its global minimum for each α_s , the χ^2 can be expressed in terms of the best-fit PDF parameter combination \mathbf{a}_0 as (see Eq. (B8) in [16])

$$\min_{\mathbf{a}} \chi^2(\mathbf{a}, \alpha_s, \{m_q\}) \equiv \chi^2(\mathbf{a}_0, \alpha_s, \{m_q\}) = \sum_E \left[\underbrace{\sum_{k=1}^{N_{\text{pt}}^{(E)}} [r_{0,k}^{(E)}]^2}_{\equiv D^2} + \underbrace{\sum_{\alpha=1}^{N_\lambda^{(E)}} [\lambda_{0,\alpha}^{(E)}]^2}_{\equiv R^2} \right], \quad (2.4)$$

i.e., it is a quadrature sum of the best-fit data residuals $r_{0,k}^{(E)}$ and best-fit nuisance parameters for each experiment E . Their explicit formulas are [16]

$$r_{0,k}^{(E)} = \frac{1}{s_k} \left(D_k - T_k(\mathbf{a}_0) - \sum_{\alpha=1}^{N_\lambda^{(E)}} \beta_{k\alpha} \lambda_{0,\alpha}^{(E)} \right), \text{ and} \quad (2.5)$$

$$\lambda_{0,\alpha}^{(E)} = \frac{1}{s_k^2} (D_k - T_k(\mathbf{a}_0)) \beta_{k\gamma} \mathcal{A}_{\gamma\alpha}^{-1}, \text{ with } \mathcal{A}_{\alpha_1\alpha_2} = \delta_{\alpha_1\alpha_2} + \sum_{k=1}^{N_{\text{pt}}^{(E)}} \frac{\beta_{k\alpha_1} \beta_{k\alpha_2}}{s_k^2}, \quad (2.6)$$

and all terms on the right-hand side corresponding to experiment E . Furthermore, since $r_{0,k}^{(E)}$ and $\lambda_{0,\alpha}^{(E)}$ are correlated only through a relatively small number of PDF parameters, especially across separate experiments, in the first approximation they all can be assumed to be independently and normally distributed, $r_{0,k}^{(E)} \sim \mathcal{N}(0, 1)$ and $\lambda_{0,\alpha}^{(E)} \sim \mathcal{N}(0, 1)$. This independence opens the possibility of reclustering the individual data points in the total χ^2 in Eq. (2.4), which will be pursued in Sec. IV. Furthermore, in Sec. IV.6 we can examine separate reclustering of sums of all best-fit residuals and nuisance parameters, denoted as D^2 and R^2 , respectively.

This reclustering procedure does not affect the best fit but can be useful for understanding stochastic effects on the resultant uncertainty, especially in connection with a dynamic tolerance prescription.

II.3. Limitations of existing models for correlated systematics

Several aspects of the implementation of correlated systematic errors through $\beta_{k\alpha}$ in our χ^2 introduced above will be relevant for interpreting the results that will follow.

1. We first note that the total number N_λ of experimental nuisance parameters has grown from at most a few tens in the early global fits to more than 2000 in the CT25 analysis. That is, N_λ is now close to a half of the total data points N_{pt} due to the tendency of the latest experiments to provide large correlation or covariance matrices. In the best fit, many of these nuisance parameters are not normally distributed, but instead cluster close to zero, leading to a spike in the distribution.
2. Each nuisance parameter is included with a prior constraint, essentially an extra datapoint preventing the parameter's completely arbitrary variations. Considerable attention has been paid recently to the fact that, by using the linear Gaussian models to publish their correlated systematic uncertainties, experiments unavoidably leave out critical information or introduce spurious assumptions that may proliferate when the number of priors is large. There are a couple such points, first, related to the standard assertion that all systematic nuisance parameters follow the standard normal distribution, $\lambda_\alpha^{(E)} \sim \mathcal{N}(0, 1)$ in the χ^2 definition in Eq. (2.3). Not only is it highly unlikely that

all λ_α parameters will be thus distributed, but there are also known important cases where this assumption is false, e.g., for so-called two-point uncertainties that take the difference of at most two estimates, for instance, provided by two parton shower programs, as a measure of a possible uncertainty [64].

3. The second point of the information loss emerges from the common practice of publishing only *normalized* correlation matrices, $\sigma_{k\alpha}$, from which the actual correlation matrices, $\beta_{k\alpha} = X_k \sigma_{k\alpha}$ in Eq. (2.3), must be reconstructed by multiplying by unspecified reference values X_k that are chosen within the PDF fit itself. The X_k values are of order of either the central data values, D_k , or respective theoretical values, T_k . They do not need to coincide with either; the prescription for choosing X_k is a delicate part of the fitting model [65, 66], approached differently by each PDF fitting group [67, 68], who try to reasonably fill the lacunas in the correlation models they get.

How do these considerations impact the precise determination of the QCD coupling constant? The next section offers some answers, after discussing another potential source of uncertainty due to the freedom in the PDF parametrization.

III. SOURCES OF UNCERTAINTIES ON QCD COUPLING

III.1. The PDF parametrization uncertainty is small...

It has been pointed out over years, e.g., in [15, 16, 69, 70], that QCD parameters determined from a global fit are mutually dependent on the PDFs and thus must be fitted simultaneously with the PDFs. Within the global fit, the correlation between the α_s and PDFs can be captured either by fitting them together or by scanning the $\chi^2(\alpha_s, \mathbf{a}_0(\alpha_s))$ over α_s , while minimizing the χ^2 with respect to the PDFs for each α_s value. Either approach can be used to determine the best-fit combination of α_s and PDFs together with their uncertainties. We will employ both, especially the latter one – the α_s scan.

Perhaps unexpectedly, our study found a low correlation between the best-fit α_s and the functional forms of PDF parametrizations in the vicinity of the overall global χ^2 minimum. The consequence is that the choice of the PDF parametrizations has a low impact on the α_s and its error, among the candidate functional forms of the CT25 fit that render the lowest achieved values of χ^2 . The variation of the best-fit α_s caused by the choice of the parametrization forms is comparable to the uncertainty corresponding to a $\Delta\chi^2 = 1$ change in the global χ^2 . We will see that this is quite a small uncertainty compared to other sources.

Figure 1 illustrates the low correlation of best-fit α_s and PDFs by comparing the χ^2 dependence

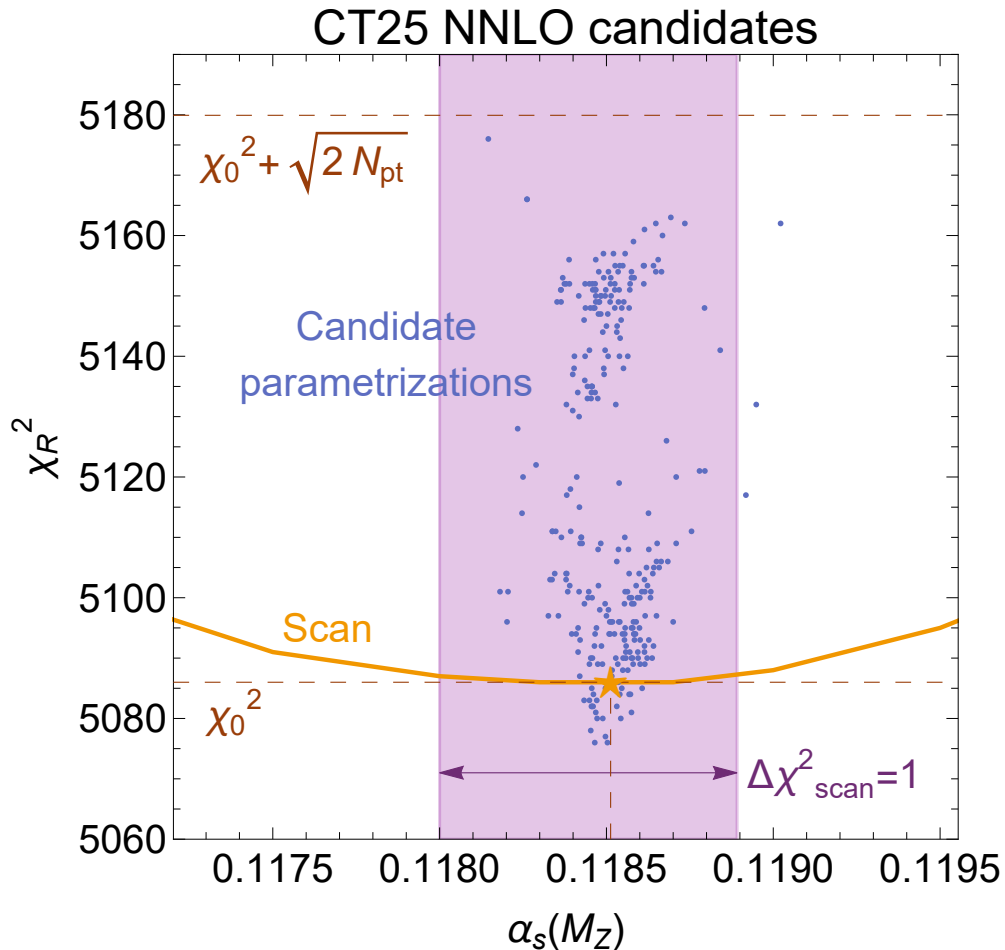


FIG. 1. χ^2 of the data versus $\alpha_s(M_Z)$ from the scan of the nominal CT25 PDF functional forms and PDF+ α_s fits with 287 alternative parametrizations.

from an α_s scan for the functional forms of the nominal CT25 fit and 287 fits with alternative PDF parametrizations explored as a part of the full CT25 exercise. In this plot, we focus on the component of the total χ^2 consisting from experimental log-likelihoods and denoted by χ_R^2 as in Eq. (2.1), and neglecting the prior component χ_{LM}^2 that is relatively constant in this comparison. All fits in this figure are done with identical settings that are close both to the CT25prel and final CT25 ones introduced in Sec. II.1. Namely, the shown fit with the nominal CT25 parametrization achieves $\min \chi_R^2 \equiv \chi_0^2 = 5087$ for $N_{pt} = 4260$ data points. Compared to the CT25prel fit, it excludes the CDHSW heavy-nucleus CC DIS data set [34], which prefers a low α_s , as well as the weakly sensitive H1 F_L data set [38]. It retains other experiments of the CT25prel baseline.

The orange star in Fig. 1 indicates the best-fit combination $\{\alpha_s \approx 0.1185, \chi_R^2 = 5087\}$ obtained with the nominal CT25 parametrization. The orange curve indicates the χ_R^2 dependence from the α_s scan with this parametrization. This curve closely follows the parabolic behavior. The vertical magenta band

indicates the interval of α_s values corresponding to the increase $\Delta\chi_R^2 \leq 1$ from the α_s scan, measured with respect to the minimal χ_R^2 on this quasi-parabola.

The blue dots indicate the best-fit $\{\alpha_s, \chi_R^2\}$ combinations from simultaneous PDF+ α_s fits that use 287 variants of PDF parametrization forms. In these parametrizations, both the functional forms and the number of parameters are varied. A small number of candidate fits in Fig. 1 have a lower χ_R^2 (slightly better agreement with data) than the nominal CT25 parameterization (the orange star). Yet they have a slightly worse overall χ^2 due to the additional LM penalties in the extrapolation regions, e.g. because they result in less physical asymptotic behaviors of (anti-)quark PDFs in the far $x \rightarrow 1$ limit. On the side of the upper χ_R^2 , we show only the candidate parametrizations that have only a modestly higher χ_R^2 compared to χ_0^2 of the nominal fit. Namely, we show the fits whose χ_R^2 is less than $\chi_0^2 + \sqrt{2N_{\text{pt}}}$, i.e., fall within the 68% CL of the statistical uncertainty on χ_R^2 of the nominal fit. Such candidate solutions are a priori eligible for inclusion into the final α_s average over PDF models, even though they would be included with a lower weight into the model average because of their elevated χ_R^2 's.

Here we observe a striking behavior: while the χ^2 variations among the candidate fits are sizable in the vertical (χ^2) direction, they have modest horizontal variations, compatible with the size of the $\Delta\chi^2 = 1$ interval, as far as the best-fit α_s are concerned. The picture immediately reminds of the textbook case of the χ^2 variability due to approximately Gaussian random fluctuations in data [71]: when one plots the log-likelihood (χ^2) vs. the parameter of interest, e.g., α_s , vertical fluctuations of the resulting parabola fall into the interval $\chi_R^2 \leq \chi_0^2 + \sqrt{2N_{\text{pt}}}$ in $\approx 68\%$ of cases, while about 68% of the horizontal fluctuations fall within the interval $\Delta\chi_R^2 \leq 1$.

In our example, the best-fit α_s from fits with alternative parametrizations fall within the $\Delta\chi_R^2 = 1$ interval from the scan, reflecting statistical fluctuations in the data at 68% CL for the fixed data set and PDF functional forms. This interval corresponds to the uncertainty $\delta\alpha_s \approx \pm 0.0005$, and this conclusion holds for other candidate selections of baseline experiments. Namely, while the preferred α_s value moves from ≈ 0.1177 for the CT25prel to 0.1185 for the CT25 selection of data sets, see the bottom of Table I, the pattern of the parametrization dependence is about the same in these fits as in Fig. 1, with the parametrization uncertainty staying at the level of 0.0005.

The conclusion based on the ensemble of nearly 300 PDF parametrizations is then that they give very similar α_s values, showing that the determination of α_s is essentially independent of the chosen PDF parametrization. If only this source of uncertainty were considered, the uncertainty span of approximately ± 0.0005 about the central value would be smaller than both the PDG uncertainty [72] of ± 0.0009 and errors of order ± 0.002 quoted by dedicated PDF-only fits [16, 17, 19, 20, 73–75]. Given these observations, the final α_s uncertainty estimate does not include a component arising from PDF parametrizations.

III.2. ...but the systematic uncertainty remains

The global fit contains two additional notable sources of α_s uncertainties: (1) the dependence on the models of correlated systematic errors discussed in Sec. II.3 and (2) the tensions between preferred values of α_s from the separate categories of data sets. This section addresses the first aspect and illustrates the possible impact of the choice of the reference normalization factors X_k in the experimental correlation matrices $\beta_{k\alpha} = X_k \sigma_{k\alpha}$, which is controlled in our fit by the parameter `ksys`. Section IV will follow with addressing the second aspect.

Since the experiments normally do not publish their recommended X_k , a variety of “guesses” about X_k can be, and have been, made in the past PDF fits [65, 66]. As illustrative possibilities, we consider two such prescriptions, which we label as “`ksys=1`” and “`ksys=2`”. According to the `ksys=1` prescription, each correlated systematic element $\beta_{k\alpha}$ (initially provided as a percentage fraction $\sigma_{k\alpha}$) is normalized to the current theory prediction T_k for each data point. This treatment is more suitable when the corresponding experimental error is multiplicative. Major systematic errors for the LHC experiments, for example jet energy scale systematic errors, are treated as multiplicative by the experiments.⁴ On the other hand, this

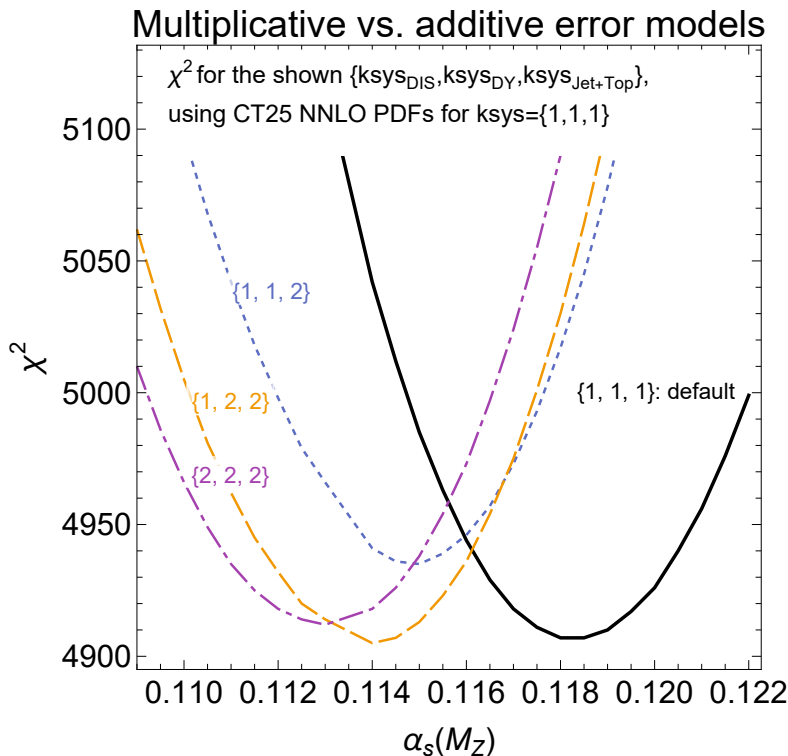


FIG. 2. χ^2 profiles for different `ksys` settings: $\{\text{ksys}_{DIS}, \text{ksys}_{DY}, \text{ksys}_{\text{Jet}+t\bar{t}}\} = \{1, 1, 1\}, \{1, 1, 2\}, \{1, 2, 2\},$ and $\{2, 2, 2\}$. These are obtained with a fixed CT25 PDF set determined with the default `ksys=1` setting.

⁴ The luminosity error of LHC inclusive jet cross sections is treated as additive.

prescription can introduce a theory bias in the effect of systematic errors, reflected e.g. in the dependence on the version of the “ t ” method for normalization of correlated errors seen in the past analyses [68]. The majority of fits by CTEQ-TEA and other groups choose `ksys=1` for all correlated errors as a default.

The `ksys=2` prescription, instead, normalizes the correlated systematic element to the experimental central value D_k . It is most suitable for normalizing additive errors. It can potentially lead to a large D’Agostini bias [67, 76, 77] (characteristically producing a downward bias in the best-fit cross section) when the underlying error is multiplicative.

For the ensuing discussion, we divide our baseline data set of measurements into three subsets: 1) deep-inelastic scattering (DIS), 2) Drell-Yan (DY) pair production, 3) inclusive jet and $t\bar{t}$ production. In each subset, we normalize all $\beta_{k\alpha}$ as though they are multiplicative (`ksys=1`) or additive (`ksys=2`), with the caveat that the `ksys=1` option is more likely to be closer to the truth. Measurements do contain a mix of multiplicative and additive errors. The true value of α_s extracted from the global fit is somewhere between the extremes corresponding to the “all `ksys=1`” and “all `ksys=2`” options, but likely closer to `ksys=1`. This setup allows us to explore sensitivity to systematic error modeling, particularly for hadron jet production observables that exhibit a very large sensitivity.

III.2.0.1. Impact of systematic-error normalizations for fixed PDFs. We first demonstrate what happens in the final CT25 fit when we change the default setting of using “`ksys=1`” in all three measurement categories, labeled as $\{\text{ksys}_{DIS}, \text{ksys}_{DY}, \text{ksys}_{\text{Jet}+t\bar{t}}\} = \{1, 1, 1\}$. First, to illustrate how the `ksys` choice modifies χ^2 when all other settings are unchanged, let us examine the χ^2 dependence for several combinations of `ksys` values *while using the same PDF ensemble*. Figure 2 illustrates these changes, by showing χ^2 vs α_s computed with $\{1, 1, 1\}$, $\{1, 1, 2\}$, $\{1, 2, 2\}$, and $\{2, 2, 2\}$ `ksys` choices, each using the same nominal CT25 data set and best-fit PDFs obtained with $\{1, 1, 1\}$.

Both the minimal χ^2 and best-fit α_s values change according to the `ksys` choices, covering the ranges of 4880-4530 and 0.1155-0.1185, respectively. The minima of the parabolas in this case correspond to the following α_s values: $\{1, 1, 1\} \rightarrow 0.1185$, $\{1, 1, 2\} \rightarrow 0.1150$, $\{1, 2, 2\} \rightarrow 0.1140$, and $\{2, 2, 2\} \rightarrow 0.1130$. The change from `ksys=1` to 2 for jet+ $t\bar{t}$ data sets alone incurs a significant downward α_s shift, which is further amplified by using `ksys=2` for the other two groups of processes.

It is interesting to investigate further into the details of the fits to understand the driving mechanism of these shifts. First, it can be noted that, as far as the α_s dependence goes, the data-point residuals are more responsive to the form of the systematic errors than the best-fit nuisance parameters. This can be seen from Fig. 3 that separately plots the contributions from the best-fit residuals and nuisance parameters, given respectively by two sums on the right-hand side of Eq. (2.4), from the same four α_s scans with the fixed $\{1, 1, 1\}$ PDF as in Fig. 2. The curves from the four scans are stacked on top of one

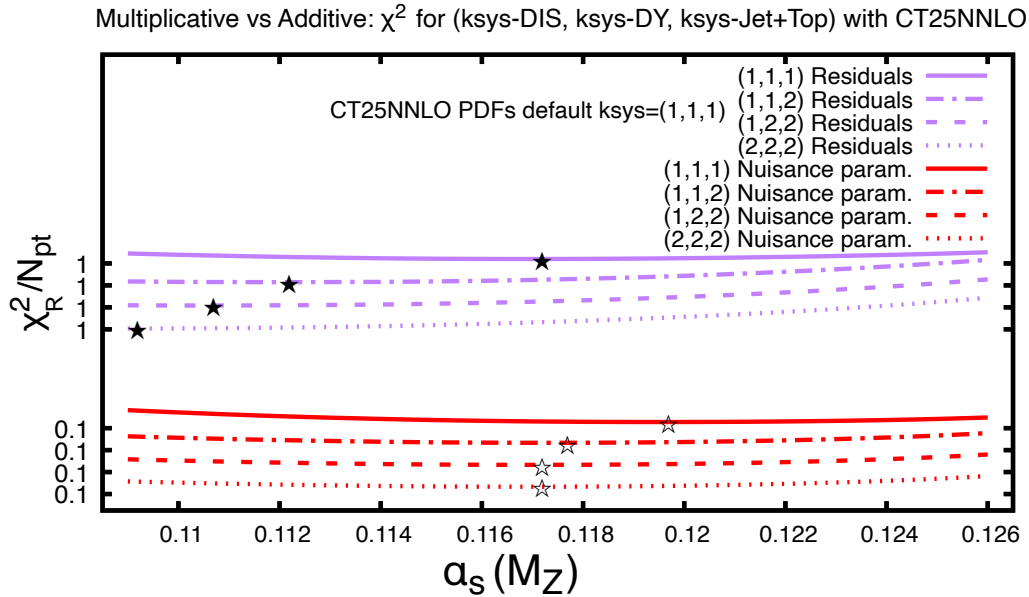


FIG. 3. Separate contributions to χ_R^2/N_{pt} from the best-fit summed data residuals and nuisance parameters, as exemplified in Eq. (2.4), for the four ksys combinations shown in Fig. 2. The theory predictions are obtained with the CT25NNLO PDFs determined using $\text{ksys}=\{1,1,1\}$.

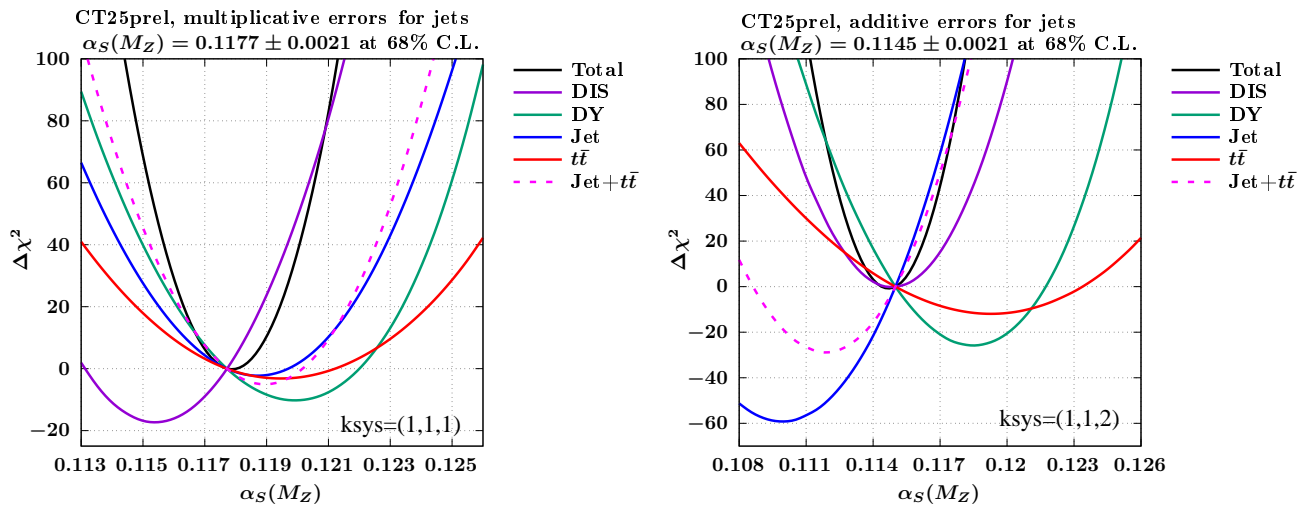


FIG. 4. Left: $\Delta\chi^2$ profiles vs. $\alpha_s(M_Z)$ for $\text{ksys}=1$ applied to all data sets. Right: same, with $\text{ksys}=2$ applied to jet data sets, $\text{ksys}=1$ to the rest. Curves are shown for the full-baseline global fit (black), DIS (purple), DY (green), jets (blue), $t\bar{t}$ (red), and jet+ $t\bar{t}$ (dashed magenta). Each parabola is obtained from the same global fit result, projected onto the corresponding data subset.

another so as to fit in the figure. Stars indicate the minima of their corresponding parabolas. Positions of the stars for residuals can go as low as $\alpha_s(M_Z) = 0.109$ for $\{2, 2, 2\}$. The stars for the nuisance parameters stay between 0.117 and 0.120.

III.2.0.2. Impact of systematic-error normalizations with fitted PDFs. Figures 4 and 5 depict this dynamics in the complete α_s scans, now done using the CT25prel baseline data set that prefers a slightly lower $\alpha_s(M_Z) < 0.118$. In these figures, the PDFs are fitted for the indicated **ksys** and α_s .

Figure 4 illustrates how the χ^2 's for groups of data sets in the CT25prel baseline vary in an α_s scan with **ksys** = {1, 1, 1} in the left subfigure and {1, 1, 2} in the right one. The curves depict $\Delta\chi^2 \equiv \chi_R^2(\alpha_s) - \chi_{R,0}^2$ vs. α_s – the changes in χ_R^2 compared to a reference value $\chi_{R,0}^2$ – for six different groups of data sets in the CT25prel fit: the full baseline (black line), DIS (purple), Drell–Yan pair (green), inclusive jet (blue), and $t\bar{t}$ production (red), as well as the combined jet+ $t\bar{t}$ data (dashed magenta). All curves are obtained in one scan in each subfigure. The reference value, $\chi_{R,0}^2$, is the minimum χ_R^2 with respect to both α_s and PDFs. By construction, the $\Delta\chi^2$ curves for all groups of processes intersect (are equal to zero) at the best-fit α_s of the global fit. The minima of the parabolas represent the preferred α_s values for each group of processes.

With the CT25prel baseline, the default global fit, using the **ksys=1** treatment (left panel), gives

$$\alpha_s(M_Z) = 0.1177 \pm 0.0021 \quad (68\% \text{ CL}), \quad (3.1)$$

where the 68% CL is computed according to $\Delta\chi^2 = 37$, the increase in the global χ^2 consistent with the CT18 tolerance definition. This α_s value is in good agreement with the current world average. At the same time, we observe that the preferred α_s values vary across the processes. For example, the DIS experiments prefer the lowest value ($\alpha_s(M_Z) = 0.1152$).⁵ Drell–Yan pair and top-quark pair production prefer higher values, 0.1198 and 0.1194, respectively. Inclusive jet production prefers an intermediate value ($\alpha_s(M_Z) = 0.1187$). The spread of preferences in Fig. 4 (left) reflects the differing pulls on α_s from various experiments and highlights tensions in the data.

When the **ksys=2** prescription is applied to the jet data only in Fig. 4 (right), the global minimum of total χ_R^2 prefers a much lower value,

$$\alpha_s(M_Z) = 0.1145 \pm 0.0021 \quad (68\% \text{ CL}). \quad (3.2)$$

In this scenario, the ordering of preferred values is markedly different: jet production measurements favor by far the smallest value ($\alpha_s(M_Z) = 0.1099$), $t\bar{t}$ production still pulls toward the largest value ($\alpha_s(M_Z) = 0.1191$), and DIS ($\alpha_s(M_Z) = 0.1146$) and Drell–Yan process ($\alpha_s(M_Z) = 0.1187$) lie in-between. Compared to the **ksys=1** case, the pull from jet-production measurements to a significantly lower value of α_s is accompanied by an equally significant reduction in the jets' χ^2 , which reflects strong sensitivity of these measurements to the treatment of correlated systematics.

⁵ In the CT25 fit, the majority of DIS experiments prefer $\alpha_s(M_Z) < 0.118$, but this preference is especially pronounced for the HERA DIS data at $Q < 3.5$ GeV and BCDMS F_2^p data.

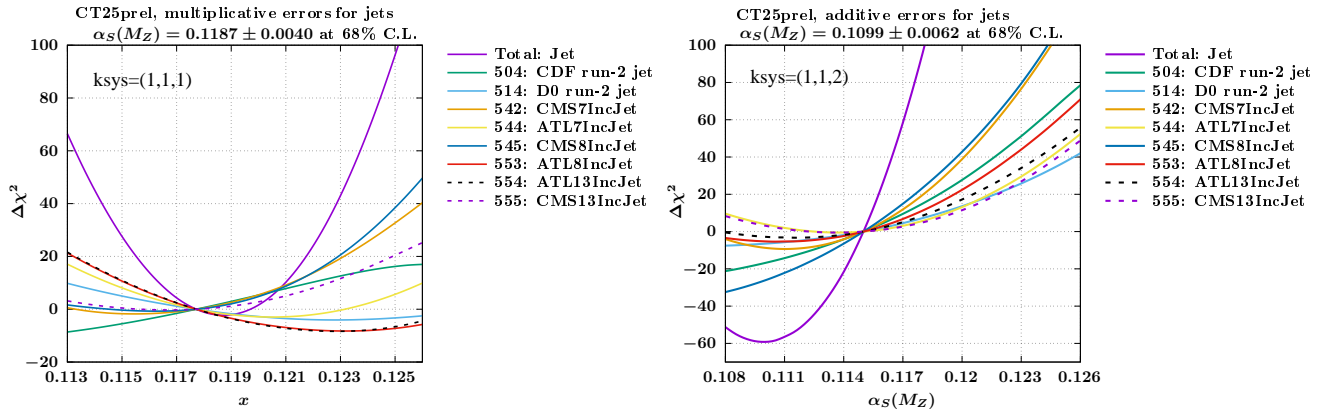


FIG. 5. $\Delta\chi^2$ profiles for individual jet-production measurements only in the α_s scans with the **ksys**=1 (left) and **ksys**=2 (right) prescriptions for jet data sets. The $\alpha_s(M_Z)$ values in the plot headers are for the jet data subset only.

To further investigate the differences between the **ksys**=1 and **ksys**=2 scenarios in the case of inclusive-jet production measurements (in the CT25prel fit), Fig. 5 separately illustrates the $\Delta\chi^2$ profiles of individual jet experiments. As before, the curves have $\Delta\chi^2 = 0$ at the best-fit α_s of the respective global fit. The **ksys**=1 case is shown in the Fig. 5 (left), where the $D\bar{O}$ Run-2 and ATLAS measurements at 7, 8, and 13 TeV collision energies prefer relatively large α_s , while the CDF Run-2 and CMS measurements at 7, 8, and 13 TeV prefer smaller values. Their interplay produces a combined α_s -minimum from jet production at

$$\alpha_s(M_Z) = 0.1187 \pm 0.0040 \quad (68\% \text{ C.L.}), \quad (3.3)$$

consistent with the world average.

By contrast, when the **ksys**=2 treatment is applied to jet data sets in Fig. 5 (right), all of them prefer a much smaller α_s . The CMS 8 TeV and CDF Run-2 data especially pull toward smaller α_s values, compared to the preference of $D\bar{O}$ and ATLAS for a somewhat larger α_s . This produces a much lower central value

$$\alpha_s(M_Z) = 0.1099 \pm 0.0062 \quad (68\% \text{ C.L.}), \quad (3.4)$$

that is well below the world average and with a larger uncertainty.

In summary, the comparison between the two different treatments for the correlated systematic uncertainties in inclusive jet production, **ksys**=1 and **ksys**=2, demonstrates that these measurements are particularly sensitive to the normalization of systematic errors.⁶ As we emphasized, requiring all correlated errors to be normalized according to the **ksys**=2 (additive) choice may exaggerate the downward

⁶ An analogous sensitivity has been noted in the NNPDF precision determination [24] of $\alpha_s(M_Z)$, whereby a fit with a floating α_s in the covariance matrix produces a higher value than the final result consistent with the additive prescription (the analog of our **ksys**=2).

pull on α_s ; however, other (theoretical) biases may be present also with the `ksys=1` prescription. Given that the major experimental errors in jet production are regarded as multiplicative, this exercise may exaggerate the possible effect, but still serves as a useful reminder of a vulnerability in the standard publication format for systematic errors.

IV. UNCERTAINTY ESTIMATION: TOLERANCES

IV.1. The $\Delta\chi^2 = 1$ criterion

The behavior of χ^2 depicted in Sec. III.2 does not yield a single answer for the uncertainty on α_s compatible with the CT25 global data. One of the conclusions from Sec. III.2 is that, regardless of the implementation of the experimental correlation models, we observe a larger-than-normal spread among α_s preferred by different classes of experiments (DIS, DY, and Jet and top-quark pair production (Jet+ $t\bar{t}$) combined), as quantified by the positions of the minima of their χ^2 profiles in Fig. 4. Consequently, several uncertainty estimates are reasonable.

We first observe that the dependence of the total χ^2 observed in our α_s scans, such as the one showed by the solid line in Fig. 1, is highly consistent with a parabolic fit, with the logarithmic derivative $d \ln \Delta\chi_R^2 / d(\ln \alpha_s - \alpha_{s,0})$ staying in the range 1.9-2.2 over the interval $\alpha_s(M_Z) = 0.110 - 0.125$ covered in the CT25 scan. Based on the total χ^2 , the standard deviation is estimated as $\delta_{68\%}\alpha_s(M_Z) \sim 0.0004$ either from the quadratic fit $\chi^2 = 6.695 \cdot 10^6 (\alpha_s(M_Z) - 0.1183)^2$ or from the condition $\Delta\chi^2 = 1$ applicable for a single-parameter probability distribution [71].

The $\Delta\chi^2 = 1$ uncertainty is interpreted as the frequentist 68% central confidence interval on the “ α_s parameter” determined from imaginary repetitions (replicas) of the same experiments using the same fitting methodology. Each such replica consists of the same selection of data points, which differ only in their random fluctuations within Gaussian uncertainties of the input measurements.

But, this surrogate parameter may differ from the true α_s realized in nature if the input data are inconsistent. Such tensions reveal non-negligible data selection uncertainty, which is a part of the model (epistemic) uncertainty.

Not only is the $\Delta\chi^2 = 1$ uncertainty ≈ 0.0004 smaller the world average quoted in the PDG [72]; by such measure the discrepancies among the input α_s values from different classes of processes are truly significant. In particular, we noticed that the DIS measurements show a large disagreement with DY and Jet+ $t\bar{t}$ measurements. This behavior reflects the presence of tensions within the CT25 global data set, which can also be seen at the level of individual data sets.

When theory perfectly agrees with data, the χ_E^2/N_{pt} ratios of individual experiments fluctuate around

the expectation of one with a known probability. What is actually seen in all global fits is that the spread of χ_E^2/N_{pt} is wider than this normal distribution arising from purely stochastic fluctuations. One can demonstrate this enlargement of discrepancies by considering histograms of effective Gaussian variables S_E constructed from χ_E^2 [16, 39]. While, in the absence of tensions, the distribution of S_E is consistent with the standard normal distribution $\mathcal{N}(0, 1)$, the empirically obtained histograms of S_E for the CT, MSHT, and NNPDF global fits are wider than $\mathcal{N}(0, 1)$ [25].

In this and the following section, we compare several strategies to account for the data selection uncertainty. First, we focus on traditionally used methods that increase the input uncertainties or introduce tolerance on the final uncertainty to address incomplete knowledge of the underlying model. Then, we apply Bayesian methods to tackle mutual consistency of the individual α_s determinations.

1. Section IV.2 applies the Particle Data Group (PDG) prescription for combining inconsistent measurements.
2. Sections IV.3 and IV.4 review the global and dynamical tolerance prescriptions; in Sec. IV.5, we explore stability of the dynamic tolerance with respect to clustering of data points.
3. Section IV.6 explores the impact of data reclustering on the α_s uncertainty.
4. Section V estimates the α_s uncertainty using a Bayesian hierarchical model and Bayesian model averaging.

IV.2. The Particle Data Group prescription

In order to quantify the level of tension, we first consider a simple combination of the α_s central values and uncertainties obtained from the three classes of experiments analyzed in Sec. III.2, namely DIS, DY, and Jet+ $t\bar{t}$ combined. We analyse $\Delta\chi_R^2$ profiles for the CT25 baseline, like those in Fig. 4, and treat the α_s values corresponding to the minima of the individual profiles as independent determinations.⁷ We find that the associated uncertainties for each class of experiments are nearly Gaussian as well, since each χ^2 profile for the i -th class is well approximated by a quadratic function

$$\chi^2(\alpha_s, \alpha_{s,i}, \sigma_i) = \frac{(\alpha_s - \alpha_{s,i})^2}{\sigma_i^2}, \quad (4.1)$$

with free parameters $\alpha_{s,i}$ and σ_i denoting the central value and uncertainty. Table II lists preferred $\alpha_{s,i}$ and σ_i , as well as their combination given by the weighted average. The combination value $\bar{\alpha}_s = 0.1184 \pm 0.0004$

⁷ Although the χ^2 profiles here are extracted from a global fit, we argue that this approximation is reasonable for the present analysis.

	DIS	DY	Jet+t \bar{t}	Weighted average
$\alpha_{s,i}(M_Z) \times 10^3$	115.14	118.62	120.65	118.37
Error ($\sigma_i \times 10^3$)	0.629	0.743	0.543	0.360

TABLE II. Individual and combined determinations of $\alpha_s(M_Z)$ from DIS, DY, and Jet+t \bar{t} data for the CT25 NNLO baseline. Errors in the bottom row are obtained with $\Delta\chi^2 = 1$.

is consistent with the respective direct determination from total χ^2 in Sec. IV.1. Again, the resulting uncertainty is significantly smaller than for the current world average [72]. More importantly, the level of tension between the input data classes is characterized by the large value of $\sum_i \chi^2(\bar{\alpha}_s, \alpha_{s,i}, \sigma_i) \approx 44$ for (3-1) degrees of freedom (d.o.f.), indicating a dramatically bad quality of the fit.

As such disagreement is unlikely to occur randomly, the Introduction of the Review of Particle Physics [72] describes a corrective approach that inflates the input uncertainties or, equivalently, defines the standard deviation to correspond to $\Delta\chi^2 = T^2$ with $T^2 > 1$. The error-inflation approach introduces a scale factor e_{SPDG} that increases the uncertainties on each individual measurement so that the reduced $\chi^2/\text{d.o.f.} \approx 1$. This condition is guaranteed by choosing the scale factor to be

$$e_{\text{SPDG}} = \sqrt{\chi^2/\text{d.o.f.}} . \quad (4.2)$$

For the combination of values in Table II, one finds $e_{\text{SPDG}} \approx \sqrt{22} \approx 4.7$. In the context of one-dimensional data combination, this condition is equivalent to adopting a global tolerance of $T \simeq 4.7$. The application of the PDG rescaling results in

$$\alpha_s = 0.1184 \pm 0.0017 \quad (\text{scaled errors, } e_{\text{SPDG}} \approx 4.7). \quad (4.3)$$

The PDG prescription rests on the premise that the nominal uncertainties must be increased when tensions suggest possible mismodeling. It is important to note that, as explicitly recommended by the PDG, such a democratic rescaling of all input uncertainties is not advised especially for fits of poor quality, when a more informed procedure should be used. For example, one could try to introduce an additional systematic error contributing only along the parameter direction affected by the tension [Sec. IV.J in Ref. 25].

IV.3. Global and Dynamical Tolerance Criteria

Nevertheless, the PDG prescription captures the broad idea that, when the control of the underlying model is in doubt, a more conservative estimate linked to testing of the models, i.e., the goodness-of-fit criterion in the frequentist paradigm, may be warranted. The tolerance prescriptions developed by the PDF analyses implement this idea.

The simplest global tolerance [78] uniformly associates the 68% CL uncertainty with an increase $\Delta\chi^2 = T^2 > 1$ along any direction in space of free parameters in the Hessian formalism. This prescription may be too simplistic, as e.g. tensions among experiments are likely to constrain different combinations of parameters in dissimilar ways. Sometimes one experiment may dominate the constraint along an orthogonal direction (an eigenvector), but more often it is a combination of experiments. The dynamic tolerance, which has been developed in several forms, leverages constraints from individual experiments to obtain T^2 values independently for each orthogonal direction in the parameter space. In this study, we examine tolerance along the direction corresponding to the α_s free parameter. We also discuss how the dynamic tolerance relates to the global and $\Delta\chi^2 = 1$ ones under reclustering of input data.

Global tolerance (GT). A common way to introduce either the global or dynamic tolerance is to consider quantiles of the probability density $P(x)$ supported on $-\infty < x < \infty$. The quantile $\xi(P, v)$ at cumulative probability v is defined by

$$\int_{-\infty}^{\xi(v)} P(x) dx = v. \quad (4.4)$$

One might consider $P(x)$ to be the χ^2 distribution of the baseline data set. Then, one determines the global tolerance T^2 , or equivalently constructs the 68% CL interval $\alpha_{s,\min} \leq \alpha_s(M_Z) \leq \alpha_{s,\max}$, from the quantile $\xi(\chi^2(N_{\text{pt}}), 0.68)$ of the χ^2 distribution with N_{pt} degrees of freedom. This is a more general procedure to compute T^2 than the PDG-inspired estimate in Sec. IV.2, as it operates directly with $P(x)$ instead of effective data points. In practice, other values of T may be implemented, such as the GT equal to the average of T values along independent parameter directions in the DT prescription.

Dynamical Tolerance (DT). When the quantiles in Eq.(4.4) are computed for each χ_E^2 profile of the individual data sets, and then a single uncertainty range is constructed from their combination, we refer to it as the ‘‘dynamical tolerance uncertainty’’ [25, 79]. Suppose the GT applied just to experiment E renders the uncertainty range $\alpha_{s,\min}^{(E)} \leq \alpha_s(M_Z) \leq \alpha_{s,\max}^{(E)}$. The DT interval for the full data set is constructed separately from the upper and lower boundaries for each experiment as

$$\alpha_{s,\min}^{\text{DT}} \equiv \max_E \alpha_{s,\min}^{(E)}, \quad \alpha_{s,\max}^{\text{DT}} \equiv \min_E \alpha_{s,\max}^{(E)}. \quad (4.5)$$

The two-tier CT18 uncertainty. The CT [39, 68] and MSHT [79] groups implement variations of this generic procedure. The global and dynamical tolerance can be combined into a more complex constraint, such as the two-tier tolerance prescription used by CT10, CT14, and CT18 PDFs. In this prescription, the global tolerance with $T^2 \sim 37$ is combined with the ‘‘tier-2’’ dynamical tolerance at the 68% CL. The goal is of the current study is to bypass this definition, which otherwise would require, in particular, to estimate the global T^2 through the quantile argument or by another means.

A simplified tolerance. We will approximate both the CT and MSHT procedures by the following simplified prescription based on the effective Gaussian variable S .

S represents a type of a Z score, i.e., it is a function of χ^2 that is distributed approximately according to $\mathcal{N}(0, 1)$ and is easier to work with than the χ^2 distribution with N_{pt} degrees of freedom. For each χ^2 , the corresponding $S(\chi^2, N_{\text{pt}})$ can be computed using either a simpler Fisher's approximation [80],

$$S(\chi^2, N_{\text{pt}}) = \sqrt{2\chi^2(N_{\text{pt}})} - \sqrt{2N_{\text{pt}} - 1}, \quad (4.6)$$

or a more precise formula by T. Lewis [81],

$$S(\chi^2, N_{\text{pt}}) = \left(-1 + \frac{1}{9N_{\text{pt}}} + \frac{1}{1 - \frac{1}{6} \ln\left(\frac{\chi^2}{N_{\text{pt}}}\right)} \right) \frac{\sqrt{18N_{\text{pt}}}}{1 + \frac{1}{18N_{\text{pt}}}}. \quad (4.7)$$

For both the CT and MSHT tolerance implementations, which are fully specified in their respective articles, the following mapping holds for the credibility interval up to subleading terms in $1/N_{\text{pt}}$:

$$\alpha_{s,\text{min}} \leq \alpha_s \leq \alpha_{s,\text{max}} \quad \Leftrightarrow \quad S(\chi^2(\alpha_s), N_{\text{pt}}) \leq S(\chi_0^2, N_{\text{pt}}) + \xi(\mathcal{N}(0, 1), v). \quad (4.8)$$

That is, the uncertainty interval at probability v is found by selecting those α_s values for which the Gaussian variable $S(\chi^2(\alpha_s), N_{\text{pt}})$ does not exceed its value $S(\chi_0^2, N_{\text{pt}})$ at the global minimum by more than the quantile $\xi(\mathcal{N}(0, 1), v)$ determined from $\mathcal{N}(0, 1)$.

The prescription (4.8) simplifies the calculation of the probability intervals, while being numerically close to the CT and MSHT full implementations. To compute uncertainties at 68% and 90% CL, one takes $\xi(\mathcal{N}(0, 1), 0.68) = 0.468$ and $\xi(\mathcal{N}(0, 1), 0.90) = 1.28$.

IV.4. Properties of the dynamic tolerance

The dynamical tolerance (DT) has proven to be convenient when accounting for constraints on PDF uncertainties from individual experiments. That said, at the detailed level, the DT has a more complicated behavior than the GT. We illustrate these aspects using the results of the α_s scans with the CT25 and CT25prel baselines described in Sec. III.

DT uncertainties neglect correlations among the data sets via the shared PDF parameters. The correlations are considered when obtaining the central prediction and neglected when estimating the uncertainty. Indeed, the global minimum that defines the central prediction arises from the correlated constraints imposed by all experiments on the PDFs. When computing the quantiles of experiments, these correlations are neglected – this approximation breaks at some level.

DT intervals tend to be asymmetric around the central value given by the position of the global minimum for all experiments. This can be explicitly seen from Eqs. (4.8) and (4.5), showing that the DT

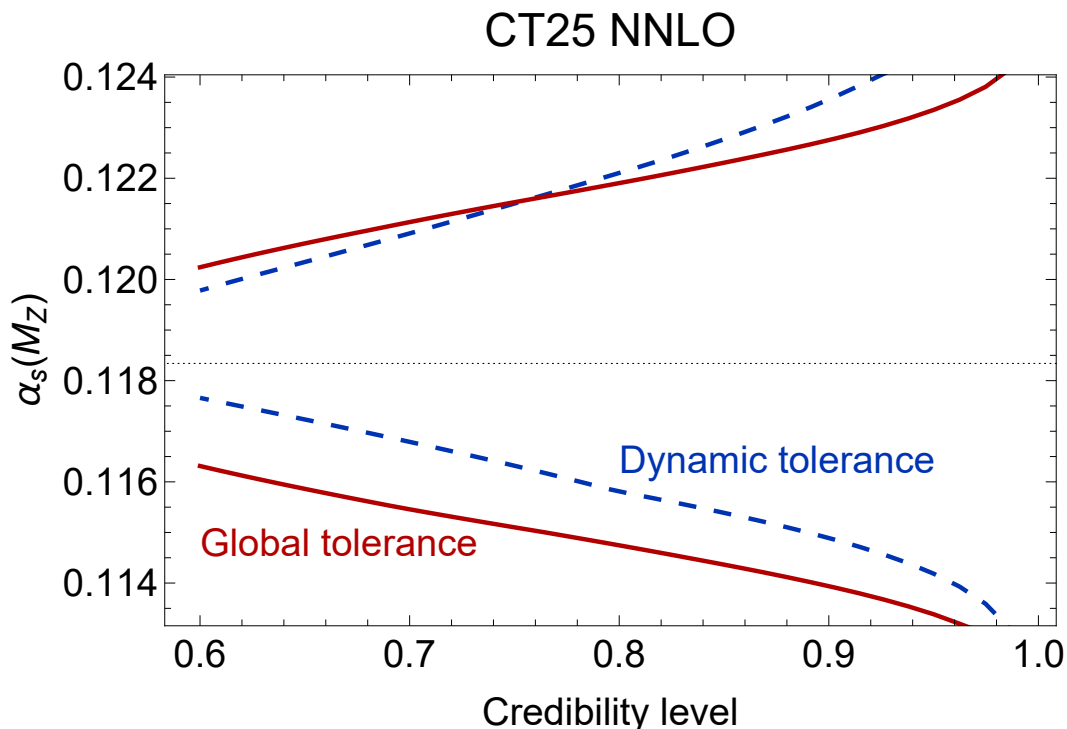


FIG. 6. $\alpha_s(M_Z)$ uncertainties in the CT25 NNLO fit as a function of the credibility level for the global and dynamical tolerance criteria. The DT error band is computed using 49 published data sets of the CT25 baseline.

intervals are determined from *changes* in the probabilities of two most constraining experiments E with respect to the global χ^2 minimum.⁸ For example, Fig. 6 compares the GT and DT uncertainties in the CT25 NNLO fit for credibility levels indicated on the horizontal axis. Throughout this article, the GT is found from the quantile of the baseline data set according to Eq. (4.4). The DT is constructed from the quantiles of 49 contributing data sets and has an obvious asymmetry above and below the central $\alpha_s(M_Z)$.

DT is sensitive to clustering of data. It depends on what counts as an independent experiment. Usually, one constructs the DT it from the χ^2 's of the published data sets. It could be equally constructed from some other clusters of data, e.g., by combining (clustering) the published data sets into “supersets” or dividing them into “subsets”.

Figure 7 shows the same default GT and DT uncertainties for the 49 data sets as in Fig. 6. In addition, we recomputed the DT 10000 times, every time randomly combining the 49 data sets into 24 clusters in the left subfigure and into 3 clusters in the right one. For every CL value, we thus quantify the uncertainty on the DT uncertainty, communicated in the figure by the filled blue bands containing 6800 instances of the re-clustered DT intervals, as well as the dotted blue bands (envelopes) indicating

⁸ In the complete the CT or MSHT implementations of the DT formulas, such behavior is achieved by applying the quantile to the ratio $S(\chi_E^2)/S(\chi_{E,0}^2)$ or $\chi_E^2/\chi_{E,0}^2$, not to $S(\chi_E^2)$ or χ_E^2 itself.

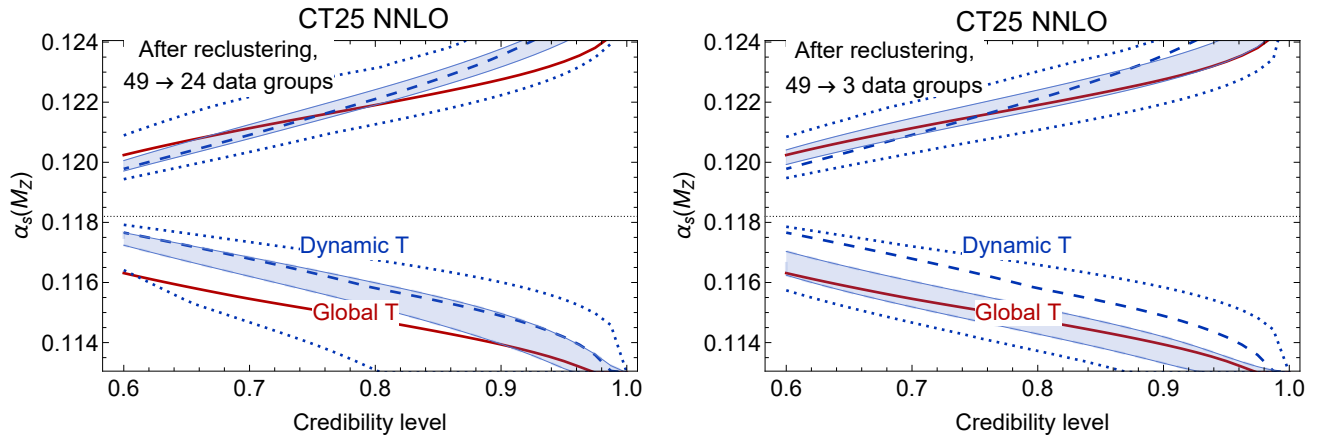


FIG. 7. Dependence on the dynamic tolerance uncertainties on the clustering of experiments in the CT25 NNLO fit. The red solid and blue dashed curves indicate the same GT and DT uncertainties as in Fig. 6. On the top we superimpose DT uncertainties from 10000 alternative clusterings of experiments in which the 49 original data sets were randomly combined in 24 clusters (left) and 3 clusters (right). At each credibility level, 6800 instances of the revised DT uncertainties fall within the light-blue bands. Blue dotted lines indicate the most extreme DT uncertainties among the 10000 instances. On average, the span of the DT errors reduces with more clusters and approaches the GT error with fewer clusters.

the most extreme instances among the 10000 re-clustered DT intervals. From Fig. 7, it is clear that the average length and uncertainty of the DT interval depend on reclusterung. Fewer clusters result in a DT uncertainty closer to the GT uncertainty, corresponding in this example to a single global data cluster. Conversely, finer clustering reduces the DT uncertainty interval.

Furthermore, we expect that clustering a pair of inconsistent experiments increases the DT interval. Conversely, splitting an inconsistent experiment into two or more clusters may reduce the DT interval. The reason is that the DT measures the change in the χ^2_E compared to its value at the best fit. When an experiment E is in a disagreement, the change in its χ^2_E is steep and often nonlinear. When inconsistent experiments are combined, their combined change may be much slower than for each one individually, resulting in a larger DT error. On the other hand, an internal inconsistency of a data set may be obviated by dividing this data set into incompatible parts, which may reduce the DT error.

Figure 8 summarizes this behavior by showing the DT uncertainty at 68% CL and 90% CL for the CT25prel baseline data comprised of 52 published data sets. In addition to the GT uncertainty, corresponding to one cluster containing all data, we show the DT uncertainty for 52 published data sets, as well as for alternative clusters (both supersets and subsets) detailed in Sec. IV.6.

The figure makes it obvious that the DT uncertainty changes depending on the clustering procedure.

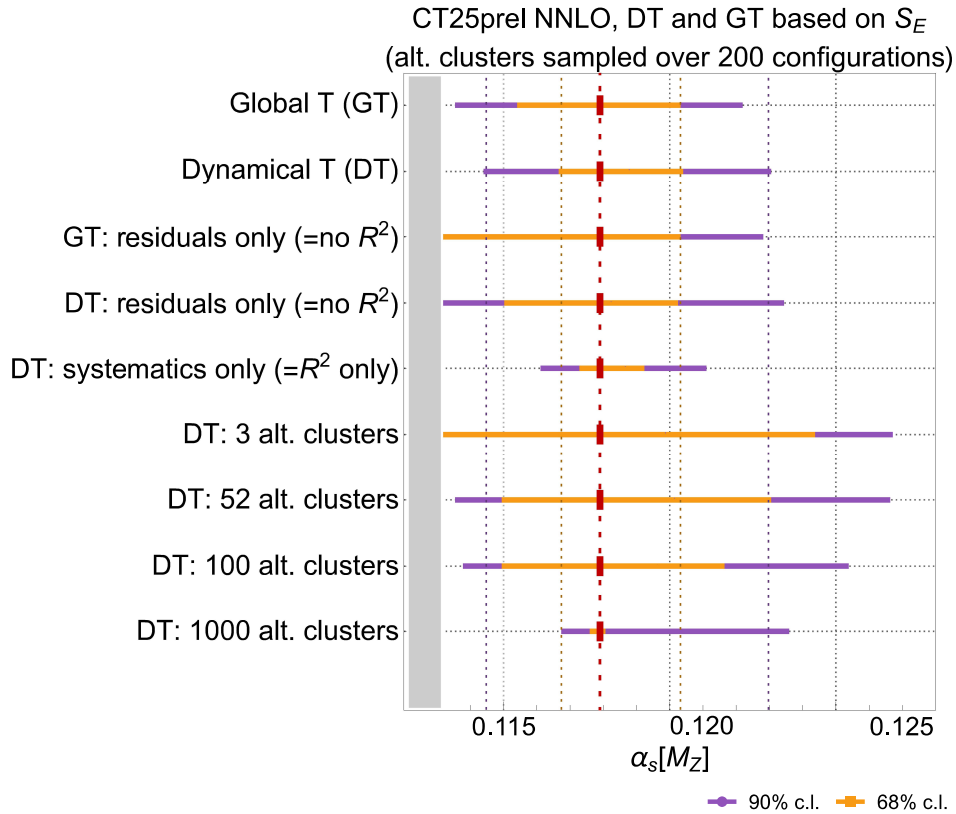


FIG. 8. Global and dynamical tolerance uncertainties on $\alpha_s(M_Z)$ at the 68% and 90% CL for various clustering procedures applied to the CT25prel baseline. DT uncertainties are estimated according to the default prescription, without and with including the sum R^2 of best-fit nuisance parameters, and optionally by reclustering the data into 3, 52, 100, and 1000 clusters as explained in Sec. IV.6. For the reclustered data, the DT errors are averaged over 200 alternative configurations.

Specifically:

$$\begin{aligned}
 \text{One cluster} & : \quad \text{DT} \approx \text{GT}; \\
 \text{Many clusters} & : \quad \text{DT} \rightarrow (\Delta\chi^2 = 1).
 \end{aligned}
 \tag{4.9}$$

When all experiments are combined, the dynamical tolerance reduces to the global one. When data are split into a large number of clusters (1000 in Fig. 8), the DT uncertainty essentially reduces to the $\Delta\chi^2 = 1$ uncertainty, when a single data point (degree of freedom) controls the allowed parameter displacement.

IV.5. Data clustering safety of uncertainty estimates

The previous subsection points out that the DT uncertainty depends on how the data are clustered. The fitting groups typically construct the DT using the full published data sets as independent clusters, but other reasonable clustering choices are obviously possible.

Such sensitivity would raise the concern that the DT uncertainty estimate on a fundamental parameter is *unsafe* at some level with respect to the user-chosen data clustering prescription. In contrast, the GT is trivially clustering-safe.

The key point here is that reclustering of the data sets modifies the degree of tensions present in the data. For instance, in a version of the CT25prel fit to 52 data sets shown in Fig. 8, the GT estimate is $\alpha_s(M_Z) = 0.1179 \pm 0.0024$, i.e. the error is practically symmetric. The default DT error, formed by the nominal clustering to the 52 data sets, is $0.1179^{+0.0024}_{-0.0011}$, showing a pronounced asymmetry. Upon reorganizing the data sets into 3 clusters, without breaking the data sets, in some cases the data sets are grouped so that their opposite pulls on $\alpha_s(M_Z)$, and in other cases these pulls are maximally exacerbated. When the tensions are largely cancelled, the 3-cluster DT error becomes nearly symmetric and larger than the GT one, e.g., $0.1179^{+0.0032}_{-0.0028}$. When the clustering magnifies the tensions, the 3-cluster DT errors vary more and can be highly asymmetric or not, for instance, $0.1179^{+0.0021}_{-0.0008}$ or $0.1179^{+0.0016}_{-0.0019}$.

The DT estimates thus in principle should be supplemented by additional tests of the degree of their clustering (un)safety. In light of what was said above, the DT errors for the α_s determination vary between zero and the GT errors. One could take an envelope of these DT errors as a conservative estimate, or an average DT error over many clustering configurations as an optimal estimate. In our specific case, the latter estimate is close to the default one using the 52 individual experiments, and hence the final uncertainty combination will concentrate on the default DT tolerance.

IV.6. Data reclustering and K-folding

It is interesting to ask whether the tolerance-based methods can quantify the impact of tensions within the available data sets, not only among the data sets. In this subsection, we further investigate this question, which is generally complex but can be elucidated by partitioning the best-fit χ^2 in Eq. (2.4) into alternative clusters of data residuals $r_{0,k}^{(E)}$ and nuisance parameters (NPs) $\lambda_{0,\alpha}^{(E)}$. This exercise reveals scaling properties of uncertainty estimates with respect to the number of clusters, although the scaling would be further affected by correlations among $r_{0,k}^{(E)}$ that are arguably less impactful and have been neglected. In particular, the estimates for GT and DT based on the residuals only (without R^2 , the contribution from NPs) are overestimated by assuming N_{pt} degrees of freedom for the contribution D^2 of the residuals instead of the actual $N_{\text{pt}} - N_{\text{par}}$. Working in this framework, we will summarize the procedure employed to partition the published data sets into many clusters illustrated in Fig. 8. Then, we will comment on the potential impact of cross validation procedures in the Monte-Carlo-based approaches on the α_s uncertainty estimate. The reader interested in the Bayesian methods and final combination can proceed directly to Secs. V and VI.

IV.6.1. Reclustering algorithm

If we neglect correlations via the PDF parameters, as was done to justify the DT to start with, then $[r_{0,k}^{(E)}]^2$ and $[\lambda_{0,\alpha}^{(E)}]^2$ from all data sets can be separately and independently collected (“shuffled”) into alternative clusters of data points, and then the DT can be formed from such clusters.

Working with the CT25prel baseline, we start by organizing all χ_R^2 components in Eq. (2.4) into two vectors \mathbf{v}_r and \mathbf{v}_λ as

$$\mathbf{v}_r = \left\{ r_{0,1}^{(1)}, \dots, r_{0,N_{\text{pt}}^{(1)}}^{(1)}, \dots, r_{0,1}^{(N_E)}, \dots, r_{0,N_{\text{pt}}^{(N_E)}}^{(N_E)} \right\}, \quad (4.10)$$

$$\mathbf{v}_\lambda = \left\{ \lambda_{0,1}^{(1)}, \dots, \lambda_{0,N_\lambda^{(1)}}^{(1)}, \dots, \lambda_{0,1}^{(N_E)}, \dots, \lambda_{0,N_\lambda^{(N_E)}}^{(N_E)} \right\}, \quad (4.11)$$

$$\text{so that } \chi_R^2 = D^2 + R^2, \quad D^2 \equiv \|\mathbf{v}_r\|^2, \quad R^2 \equiv \|\mathbf{v}_\lambda\|^2. \quad (4.12)$$

We randomly assign the \mathbf{v}_r and \mathbf{v}_λ components to N_{cl} clusters with equal numbers of data points (modulo N_{cl}), keeping this assignment same for all α_s . We construct the DT according to the same procedure as for the published data sets in Sec. IV.3. Namely, for each cluster E we compute the χ_E^2 quantile at our CL, determine $\alpha_{s,min}^{(E)}$ and $\alpha_{s,max}^{(E)}$ for this quantile, and then construct the DT bounds as in Eq. (4.5), where E now runs over the clusters. We examine the α_s dependence of DT by (a) constructing the DT interval for each of $N_{\alpha_s} = 21$ values of $\alpha_s(M_Z)$ on a grid between 0.113 and 0.129, and (b) repeating this procedure many (e.g., > 200) times, each time reshuffling the assignment of $r_{0,k}^{(E)}$ and/or $\lambda_{0,\alpha}^{(E)}$. We can compute DT for D^2 only, R^2 only, or the whole $D^2 + R^2$. We can do this because, in our approximation, the best-fit residuals and nuisance parameters enter χ_R^2 as independent degrees of freedom.

In Fig. 7, the first five lines compare the GT and DT uncertainties at 68% and 90% CL computed based on the full χ_E^2 , residuals (D^2) only, and nuisance parameters (R^2) only. This comparison reveals elevated tension in the R^2 , causing the DT uncertainty based on R^2 only (line 5) to be smaller than those based on the full $D^2 + R^2$ (line 2) and D^2 only (line 4). Appendix B further explores the GT and DT estimates collected in Fig. 7, also providing them at other credibility levels.

IV.6.2. K-folding impact on α_s

Cross validation methods such as jackknife resampling [82–84] are widely adopted to estimate the data selection uncertainty. In a classical realization, the parameter of interest is first estimated from a part (fold) of the baseline data; the parameter’s expectation value and variance are determined by averaging over multiple random selections of such folds. Cross validation is also a part of MC/ML approaches and involves partitioning the baseline data set into training, testing, and occasionally validating components. One can ask, for instance, to what extent the cross validation technique of “K-folding” deployed in the

recent NNPDF determination [24] of $\alpha_s(M_Z)$ may be sensitive to data tensions. Since K-folding involves reclustering of the baseline data, we will briefly review its possible impacts on the $\alpha_s(M_Z)$ uncertainty.

In the common K-folding procedure, each replica of the data baseline is partitioned into several folds (clusters), with one fold set aside as the test data set. The model is then trained on the union of remaining folds. A figure of merit called a “loss function” L is optimized so as to achieve good agreement with both the training and testing sets. The training procedure is iterated by excluding every fold in turn and training on the rest of the folds. In the α_s study, each such iteration also returns the best-fit $\alpha_s(M_Z)$ and its uncertainty. The final $\alpha_s(M_Z)$ is determined by weighted averaging over all replicas and K-folding iterations. The weights may be given in terms of the respective α_s uncertainties from the iterations.

In the NNPDF study [24], each replica of the published data sets is partitioned into the training set and testing fold as 3:1, without breaking the data sets apart. The α_s uncertainty from each iteration of training is determined essentially according to the $\Delta\chi^2 = 1$ criterion. The final $\alpha_s(M_Z)$ is obtained by averaging over the data replicas and K-folding iterations using $1/(\Delta\alpha_s(M_Z))^2$ from each iteration as the weight. Their resulting value $\alpha_s(M_Z) = 0.1194_{-0.0014}^{+0.0007}$. The lower of these uncertainties is roughly equal to the quadrature sum of our $\Delta\chi^2 = 1$ and PDF parametrization uncertainties. The NNPDF uncertainty is smaller than our $\delta\alpha_s \approx 0.002$, plausibly because the latter also includes the data selection uncertainty.

We posit, based on the preceding discussion, that the reclustering involved in K-folding should affect $\delta\alpha_s$. For a reliable estimate, $\delta\alpha_s$ should be averaged over a representative ensemble of K-folding/cross-validation partitions.

While such an exhaustive analysis, especially refitting the PDFs for multiple data partitions, is beyond the scope of our article, Appendix C highlights several considerations based on the following simplified exercise.

Working again with vector \mathbf{v}_r of about 4000 best-fit residuals from the CT25prel baseline, we partition the residuals into four clusters of about 1000 members each. Similarly, we partition nuisance parameters from vector \mathbf{v}_λ into four approximately equal clusters. We repeat this step 100 times, each time randomly modifying the partitions. For each partition (alternative configuration) and for the averages over 100 alternative configurations, we plot the α_s dependence of χ_R^2/N_{pt} in each cluster in Fig. 9. We make an important observation, namely, that the χ_R^2/N_{pt} distributions in Fig. 9 are flatter than would be expected from an ideal distribution of a cluster of ≈ 1000 made-up residuals that are consistently distributed according to $\mathcal{N}(0, 1)$ around a single reference value of $\alpha_s(M_Z) = 0.119$. Figure 10 shows this idealized distribution rendering a deeper parabola.

The flatter χ_R^2 of the clusters of actual residuals in Fig. 9 indicates a larger uncertainty than ≈ 0.0003 obtained by fitting the ideal parabola in Fig. 10, with the latter being in a perfect agreement with

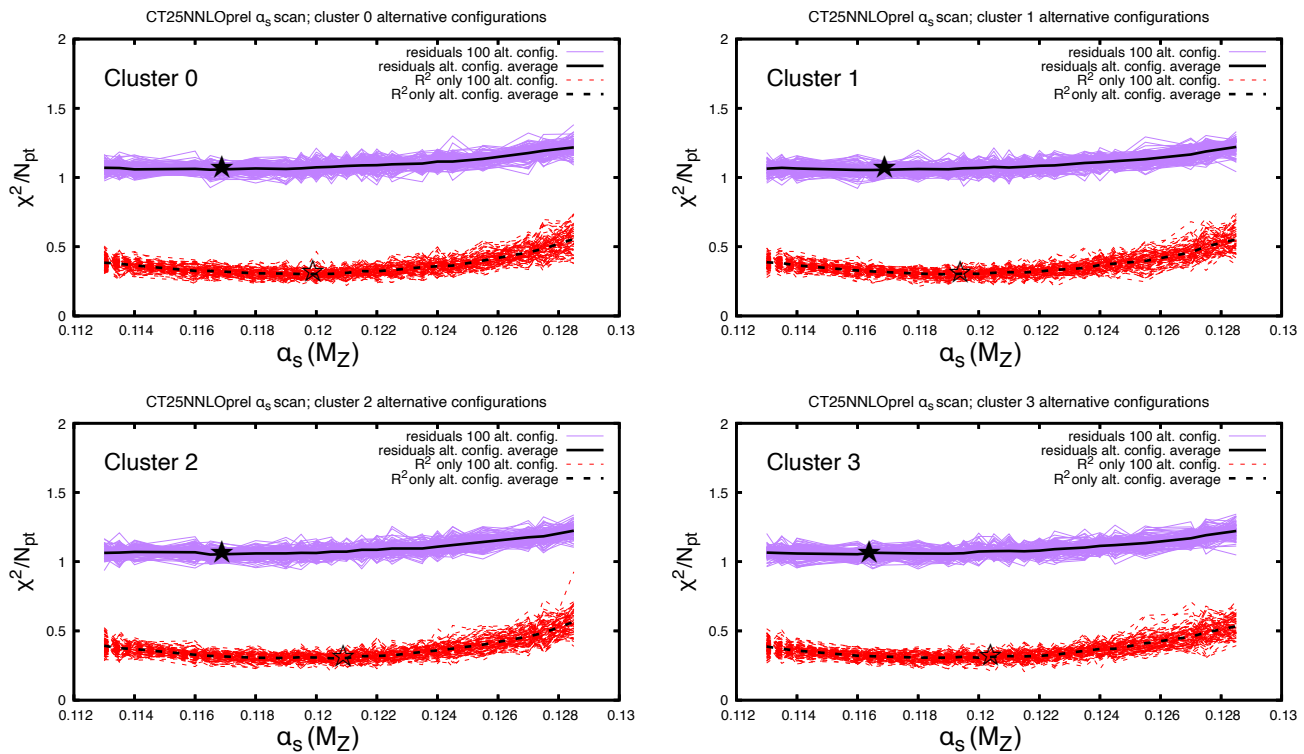


FIG. 9. χ^2/N_{pt} as a function of $\alpha_s(M_Z)$ for 100 alternative configurations of residuals and nuisance parameters partitioned into four equal-sized clusters.

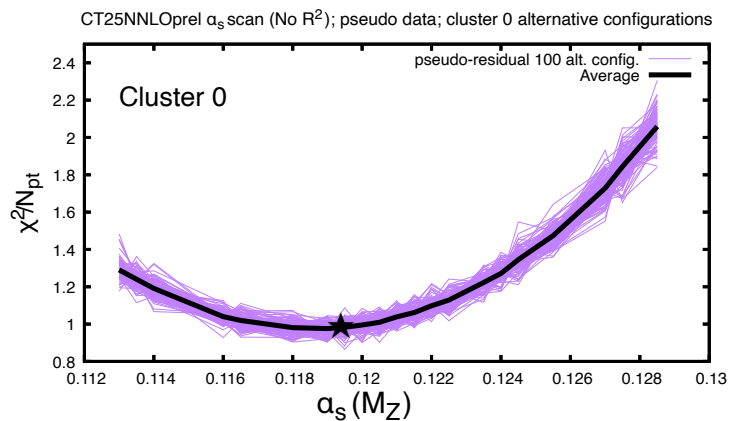


FIG. 10. χ^2/N_{pt} as a function of $\alpha_s(M_Z)$ for cluster 0 with random reshuffling of pseudoresiduals from pseudodata without tensions.

$\Delta\chi^2 = 1$. The second part of this exercise tries to estimate the actual uncertainty, keeping in mind that it depends on how the clusters are formed. To gain an insight about the practical K-folding studies, we determine $\delta\alpha_s$ from random combinations of three out of four above clusters. In this specific example, and using the DT, we find that $\delta\alpha_s$ varies between ≈ 0.0002 and 0.002 depending on the magnitude of tension in the dominant cluster of each configuration.

This exercise can be expanded in a more realistic cross-validation setup to explore the variability of $\alpha_s(M_Z)$ and its uncertainty across the full granularity of data. Appendix C contains further details, including concrete uncertainty estimates.

V. BAYESIAN MODELS FOR UNCERTAINTY ESTIMATION

The fundamental assumption of the tolerance prescriptions is that all experiments agree on the parameter of interest in a certain region, and this region can be estimated from the augmented loglikelihood by following the described procedures. In contrast, Bayesian model averaging (BMA) assumes that some experiments are more likely to be correct than others. BMA estimates the underlying probability for each experiment to be correct according to the data. In this section, we describe how two such models can be used to determine the best-fit α_s and its uncertainty, working with the CT25 baseline data set as an example. We focus on combination of α_s values preferred by DIS, DY, and Jet+ $t\bar{t}$ classes of processes summarized in Table II. As in the previous section, we make a simplifying assumption that the correlations among the separate experimental data sets via the PDFs or other parameters are negligible, allowing us to treat these data as independent α_s determinations.

V.1. A Bayesian Hierarchical Model

In combining the different values of $\alpha_{s,i}(M_Z)$ from multiple experiments, a key difficulty is that the quoted uncertainties from each experiment may not fully capture all sources of systematic error, theory assumptions, or hidden correlations. A naive combination, such as the simple weighted average in Sec. IV.2, implicitly assumes that all measurements are mutually consistent and that their reported uncertainties are complete. When this assumption fails, the resulting average can become artificially precise or biased toward experiments that happen to quote smaller, but possibly underestimated, error bars.

A Bayesian hierarchical model (BHM) provides a principled way to address this problem. Instead of treating each experimental determination $\alpha_{s,i}(M_Z)$ as an estimate of a single common parameter with known variance, the hierarchical approach acknowledges the possibility of unmodeled spread among the measurements by introducing hyperparameters that describe a latent “parent” distribution from which the individual measurements of $\alpha_{s,i}(M_Z)$ are drawn. Specifically, considering each $\alpha_{s,i}(M_Z)$ to be the result of a random draw from a parent distribution, one can write

$$p(\alpha_{s_i}) = \int p(\alpha_{s_i}|\mu, \tau)p(\mu, \tau)d\mu d\tau , \quad (5.1)$$

where $p(\mu, \tau)$ is a hyperprior distribution for the hyperparameters μ and τ .

Before introducing the specific hierarchical model used in this analysis, it is important to comment on the choice of hyperprior distribution. In Bayesian hierarchical methods, the role of the hyperprior is not to encode detailed knowledge about the data, but rather to parameterize our uncertainty about the possible degree of inter-experimental variation. While a fully data-driven determination of the hyperprior is in principle possible, it generally requires a more complex model structure. We consider two possible models, one where the choice of hyperprior is well-motivated but not derived from data (in this subsection), and the other where the hyperprior is determined through data-driven methods (in Sec. V.2).

A suitable guiding principle in choosing the hyperprior is that it should (i) be weakly informative, so that it does not dominate the posterior when the data are mutually consistent, and (ii) be flexible enough to accommodate additional dispersion among the measurements when they exhibit tension. The form proposed in Ref. [85] satisfies these requirements while avoiding ad hoc error inflation or outlier removal. It introduces a single hyperparameter τ describing the possible extra variance beyond the quoted experimental uncertainties, and assigns to it a μ -independent hyperprior,

$$p(\tau) d\tau^2 \propto \prod_{i=1}^N \left[\frac{1}{\sigma_i^2 + \tau^2} \right]^{\beta/(2N)} d\tau^2, \quad (5.2)$$

which smoothly interpolates between a flat prior ($\beta = 0$) and a sharply peaked one for larger values of β . This construction allows the analyst to encode a controlled level of prior belief about the reliability of the quoted uncertainties: smaller values of β correspond to a more permissive prior, suitable when the data exhibit significant disagreement, while larger values correspond to the assumption that most of the quoted uncertainties are reliable. This model was introduced as a more general alternative to the PDG prescription [85].

We combine the data given in Table II, according to which $N = 3$ in Eq. (5.2) represents the number of $\alpha_s(M_Z)$ measurements being combined, and σ_i are the corresponding uncertainties. For $\beta = 0$, we find $\alpha_s(M_Z) = 0.1181_{-0.0031}^{+0.0030}$. The variation of the uncertainty estimate as a function of β is shown in Fig. 11 (left), where we note that the $\alpha_s(M_Z)$ uncertainty reduces as β increases. Specifically, for $\beta = 15$ we find $\alpha_s(M_Z) = 0.1182_{-0.0007}^{+0.0006}$. Given the large spread of $\alpha_s(M_Z)$ values in Table II, and following the suggestion of Ref. [85], we use smaller values of β . Rather than choosing a single value of β , we average over $0 \leq \beta \leq 1$, which yields

$$\alpha_s(M_Z) = 0.1181_{-0.0023}^{+0.0022}. \quad (5.3)$$

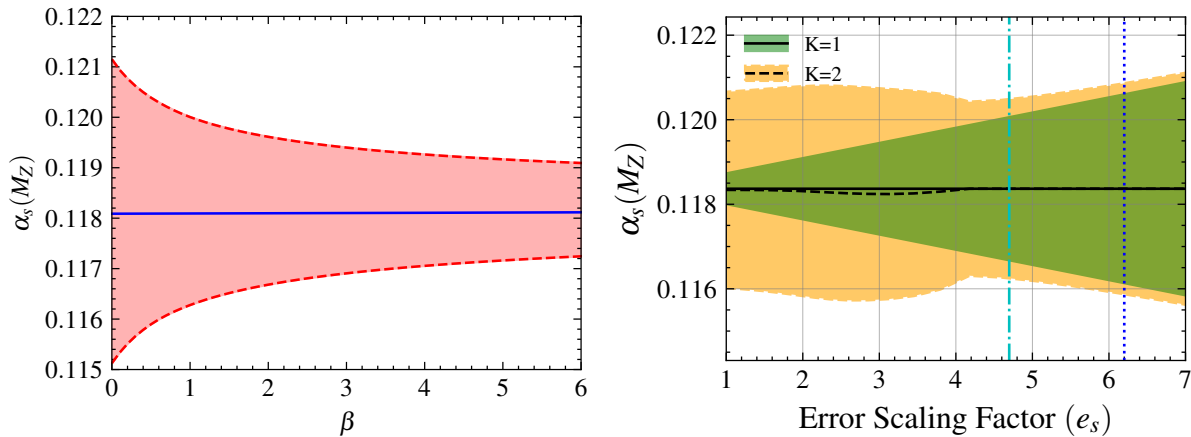


FIG. 11. Variation of the uncertainty on $\alpha_s(M_Z)$ when using the BHM (left) with a hyperprior defined in Eq. (5.2), and when using the GMM (right) as a function of the error scaling factor e_s . The orange shaded region represents the uncertainty when setting $K = 2$ in the GMM, and the green shaded region represents the uncertainty for $K = 1$, which corresponds to the usual χ^2 fit. Also shown are vertical lines indicating the values of $e_s \approx 4.7$ and $e_s \approx 6.2$, respectively corresponding to the PDG scale factor in Eq. (4.3) and tolerance T with standard combination ($K = 1$) that would give the same uncertainty estimate as the GMM with $K = 2$. For both plots, the data used in the combination is shown in Table II.

V.2. A Gaussian Mixture Model

The Gaussian mixture model (GMM) proposed in Ref. [86] is a new Bayesian hierarchical model in which the hyperprior is determined from data through the use of statistical information criteria. In this section, we summarize an application of the GMM to combine the $\alpha_s(M_Z)$ values with a large spread in Table II by capturing the multimodal feature of these data. Appendix D discusses technical aspects of this combination.

In the GMM, K Gaussian components are introduced, so that the likelihood is modeled as

$$L(\alpha_s) = \sum_{k=1}^K w_k \mathcal{N}(\alpha_s | \mu_k, \sigma_k^2), \quad (5.4)$$

where w_k are mixture weights. The optimal value of K is determined using model selection criteria such as the Akaike Information Criteria (AIC) [87] and Bayesian Information Criteria (BIC) [88]. For the present combination, the choice of $K = 2$ minimizes both the AIC and BIC. Note that $K = 1$ corresponds to the standard χ^2 combination in Table II. Minimizing the AIC score with respect to K yields a bimodal posterior for $\alpha_s(M_Z)$. Following the procedure of Ref. [86], we extract the $\alpha_s(M_Z)$ central value and its uncertainty from this distribution and find

$$\alpha_s = 0.1183 \pm 0.0023 \quad (\text{GMM}, K = 2). \quad (5.5)$$

Importantly, this estimate is obtained without inflating the errors, i.e., for the error rescaling factor $e_S = 1$. We have also examined the combination under the tentative scaling of errors by a factor $e_S > 1$. We find that the $K = 2$ combination with $e_S \approx 1$ is always preferred (has the lowest AIC score), closely followed by the traditional $K = 1$ combination with $e_S \approx 3.5$ that has a marginally higher score – see Fig. 14 in Appendix D. Thus, it would not be unreasonable to also consider the $K = 1$ case when $e_S \approx 3.5$ to determine the α_s uncertainty. This choice, however, produces a poor agreement with the input data in Table II, with a large value of $\sum_i \chi^2(\bar{\alpha}_s, \alpha_{s,i}, \sigma_i)$ as well as a too small uncertainty. We therefore do not pursue it.

Figure 11 (right) illustrates the dependence of the $\alpha_s(M_Z)$ uncertainty on e_S for both $K = 1$ (standard χ^2) and $K = 2$ (GMM). The orange and green shaded regions represent the uncertainty estimates for $K = 2$ and 1, respectively. When the errors are not rescaled, then $e_S = 1$, and $K = 1$ produces a very small uncertainty identical to the one presented in the last column of Table II. On the other hand, for this e_S value (specifically, for $e_S < 2.3$), the $K = 2$ model is preferred according to the AIC and BIC criteria. The uncertainty for $K = 1$ increases with e_S , whereas the uncertainty for $K = 2$ decreases around $e_S \approx 4.2$ and then increases linearly as in the $K = 1$ model, see Figure 11.

From Fig. 11 (right), it follows that the standard ($K = 1$) treatment reproduces the α_s uncertainty obtained with the GMM ($K = 2$) by applying $e_S \approx 6.2$, or, equivalently, adopting a tolerance T such that $\Delta\chi^2 = T^2 \approx 33$ (see Sec. IV.2 for the relation between T and e_S):

$$\alpha_s = 0.1183 \pm 0.0023 \quad (\text{scaled errors, } e_S \approx 6.2 \text{ or } T^2 \approx 33).$$

This is larger than $e_S = 4.7$ from the PDG prescription in Sec. IV.2 and slightly smaller than the effective scaling of $e_S \approx 6.9$, or $T^2 \approx 48$, that reproduces the uncertainty estimate from the global tolerance criterion defined in Sec. IV.3. In Fig. 11 (right), the values of $e_S = 4.7$ and 6.2 are indicated by vertical dot-dashed and dotted lines.

VI. FINAL COMBINATION OF α_s DETERMINATIONS

Having reviewed the physics factors affecting the extraction of α_s and several procedures to determine the α_s uncertainty, we are ready to combine this information to provide the final α_s determination.

In Sec. IV.1, we pointed out that the $\Delta\chi^2 = 1$ criterion would capture only a small part of realistic α_s uncertainty, and that an additional uncertainty must be associated with data’s internal consistency. As a reminder, when examining the χ^2 profile for the CT25prel baseline Fig. 4, the application of the $\Delta\chi^2 = 1$ criterion to the total χ^2 (black curve) would result in $\alpha_s(M_Z) = 0.11837_{-0.00041}^{+0.00035}$. This uncertainty is smaller than the global average quoted in the PDG [72].

As evidence supporting this conclusion, Sec. III.2 and Sec. IV.2 pointed out a significant spread in the minima of χ^2 profiles from different classes of experiments (DIS, DY, and Jet and top-quark pair production (Jet+ $t\bar{t}$) combined), reflecting the presence of tension between the experiments that has been also confirmed at the level of individual experiments by other techniques. We also noted the sensitivity of the χ^2 profiles to only partly known normalizations of the correlated systematic errors controlled by the `ksys` parameter. In particular, we noticed that the DIS measurements show significant disagreement with DY and Jet+ $t\bar{t}$ measurements for the default normalizations of systematic errors.

These limitations of the $\Delta\chi^2 = 1$ criterion raise the question of finding more complete procedures to quantify the uncertainty. We have explored several such procedures in Sec. IV and Sec. V. In this section we compile the results from these different prescriptions and combine them into one final estimate of the α_s central value and uncertainty.

VI.1. The central α_s value

In Sec. II, we observed that the choice between the acceptable baseline data sets affects the central α_s value. The two described baselines, CT25prel and CT25, yield the central values of about 0.1179 and 0.1184, respectively. In the following, we will quote the latter as our final α_s determination. In contrast, the choice between the baselines only weakly influences the uncertainty determination, which instead depends on the method for the estimation. In the following, we summarize the uncertainty ranges obtained with several such methods.

VI.2. Final α_s determination

The four approaches that we choose for the final combination are based on the global and dynamical tolerances, as well as on the two Bayesian models.

Global and dynamical tolerances. Sec. IV.3 described the commonly used uncertainty prescriptions based on the global and dynamical tolerance, or GT and DT. When we apply the GT criterion based on the 68% quantile for the sum of all χ_E^2 using the CT25 baseline from the individual experiments, we obtain

$$\delta\alpha_s(M_Z) = 0.1184_{-0.0028}^{+0.0026}. \quad (6.1)$$

The DT procedure results in

$$\delta\alpha_s(M_Z) = 0.1184_{-0.0014}^{+0.0023}, \quad (6.2)$$

which exhibits substantial asymmetric uncertainty.

Statistical Method	Eq.	$\delta\alpha_s(M_Z)$
Global Tolerance	6.1	$0.1184^{+0.0026}_{-0.0028}$
Dynamical Tolerance	6.2	$0.1184^{+0.0024}_{-0.0012}$
BHM	5.3	$0.1181^{+0.0022}_{-0.0023}$
GMM	5.5	$0.1183^{+0.0023}_{-0.0023}$
Average		$0.1183^{+0.0023}_{-0.0020}$

TABLE III. Estimates of $\alpha_s(M_Z)$ obtained by four distinct analyses of statistical uncertainty.

These results are obtained for the default pole mass $m_c = 1.3$ GeV of the CT25 analysis. While in principle the charm mass is correlated with the gluon PDF and therefore α_s , in practice this correlation is weak. Appendix E shows the GT and DT α_s ranges for the alternative masses 1.2 and 1.4 GeV, and those essentially coincide with the estimates for 1.3 GeV. The m_c dependence is hence found to be minimal, as is also illustrated by the χ^2 profiles in Fig. 15.

Bayesian Models. In Section V, we discussed two Bayesian models to estimate α_s uncertainties. We obtained $\alpha_s(M_Z) = 0.1181^{+0.0022}_{-0.0023}$ with the Bayesian Hierarchical Model and $\alpha_s(M_Z) = 0.1183 \pm 0.0023$ with the Gaussian Mixture Model.

The average of four methods.

Table III collects the uncertainty estimates obtained with our four methods. The last row, labeled ‘‘Average’’, corresponds to approximating the $\alpha_s(M_Z)$ probability distribution from each statistical model as a split normal distribution and summing over each model with uniform weights to produce an average. This yields a final combined average value and uncertainty of $\alpha_s(M_Z) = 0.1183^{+0.0023}_{-0.0020}$.

Good consistency among the four determinations increases our confidence in this result. It is important to emphasize that the determinations do not invoke a fixed tolerance value. Instead, they would justify a specific T^2 , should it be used as a proxy for the more complex approaches that we describe. For the CT25 baseline, the average $\delta\alpha_s(M_Z)$ in Table III translates into the $\Delta\chi^2 = {}^{+39}_{-25}$ for the global χ^2 . This is close, although not identical, to the approximate $T^2 = 37$ at 68% CL introduced in the ‘‘CT two-tier tolerance’’ prescription used in the previous CT PDF analyses [16, 68, 89].

VII. CONCLUSIONS

We have presented a new determination of the strong coupling constant $\alpha_s(M_Z)$ from the CT25 global QCD analysis at NNLO, incorporating high-precision LHC Run-2 measurements and improved statistical methodology. The global analysis simultaneously fits parton distribution functions, α_s , and other QCD parameters to a diverse collection of measurements from fixed-target and collider experiments, providing

the most complete treatment of correlations among these parameters. Our central result, combining four independent uncertainty prescriptions, is

$$\alpha_s(M_Z) = 0.1183_{-0.0020}^{+0.0023} \quad (68\% \text{ CL}).$$

This value is in good agreement with the current PDG world average and with other recent determinations from LHC data and lattice QCD.

A central theme of this work is the critical assessment of uncertainty quantification. We demonstrated that the naive $\Delta\chi^2 = 1$ uncertainty—approximately ± 0.0004 for the CT25 data set—is insufficient, because it captures only statistical fluctuations and ignores the significant tensions among the three broad classes of data (DIS, Drell–Yan, and jet + $t\bar{t}$ production). These tensions are reflected in the large spread of preferred α_s values across process types (0.1152 to 0.1198 for the CT25prel baseline with multiplicative systematic errors) and in the failure of the combination of the three classes to satisfy a standard goodness-of-fit test by a wide margin.

We investigated four methodologically distinct approaches to incorporate the full uncertainty:

- **Global tolerance (GT)**: Based on the 68% quantile of the total χ^2 distribution, yielding

$$\alpha_s(M_Z) = 0.1184_{-0.0028}^{+0.0026}.$$

It is trivially insensitive to data clustering.

- **Dynamical tolerance (DT)**: Constructed from quantiles of the individual experiment profiles, giving

$$\alpha_s(M_Z) = 0.1184_{-0.0012}^{+0.0024},$$

with a pronounced asymmetry. We showed that DT estimates depend on how experiments are grouped into clusters, and we introduced the concept of *data-clustering safety* to characterize this dependence: an uncertainty estimate on a fundamental parameter is clustering-safe if it remains stable under reasonable regroupings of the data. The GT satisfies this criterion by construction; the DT does not in general and requires supplementary tests. In the limit of a single cluster the DT reduces to the GT, while in the limit of many clusters it approaches the $\Delta\chi^2 = 1$ uncertainty.

- **Bayesian hierarchical model (BHM)**: Introducing a hyperprior that accounts for unmodeled inter-experimental spread, and averaging over the hyperprior parameter $0 \leq \beta \leq 1$, yields

$$\alpha_s(M_Z) = 0.1181_{-0.0023}^{+0.0022}.$$

- **Gaussian mixture model (GMM)**: Determining the data-adaptive hyperprior via information criteria, we find a bimodal posterior driven by multimodal structure in the data which yields

$$\alpha_s(M_Z) = 0.1183 \pm 0.0023.$$

The four methods are in good mutual agreement. Their uniformly weighted combination gives the final value quoted above, corresponding to an effective global tolerance of $\Delta\chi^2 = {}^{+39}_{-25}$, close to the $T^2 = 37$ used in previous CT PDF analyses.

We also identified systematic uncertainties that could shift the central value. The treatment of correlated systematic errors in inclusive-jet production is the most consequential: switching the normalization convention from multiplicative (`ksys=1`) to additive (`k=2`) for jet data alone lowers the global α_s by about 0.003, while simultaneously producing a large internal tension within the jet data sets and a substantially poorer goodness-of-fit. Since the major jet-energy-scale uncertainties at the LHC are regarded as multiplicative, the `ksys=1` result is preferred; nonetheless, this exercise underscores the importance of clear documentation of systematic-error conventions by experimental collaborations. We also found that the choice of PDF parametrization and variations of the charm-quark pole mass between 1.2 and 1.4 GeV have only a small effect on α_s , with the parametrization uncertainty confined to $\approx \pm 0.0005$ across 287 independent candidate parametrizations.

Looking ahead, future HL-LHC measurements will further constrain α_s and the PDFs, but the precision gains will be meaningful only if accompanied by robust uncertainty quantification. The concept of data-clustering safety introduced here provides a concrete, calculable diagnostic for the stability of uncertainty estimates based on tolerance or cross-validation methods, applicable to both Hessian and Monte Carlo PDF methodologies. Together with the Bayesian approaches discussed in this work, the proposed methodologies provide a framework for self-consistent uncertainty quantification, which is essential for a precise determination of α_s from hadron-collider data.

ACKNOWLEDGMENTS

We thank Amanda Cooper-Sarkar, Olaf Behnke, Tom Cridge, Louis Lyons, Robert Thorne, CTEQ-TEA colleagues, and participants of PDF4LHC-PHYSTAT meetings for conversations on uncertainty quantification for QCD parameters determined in PDF fits. We thank Tie-Jiun Hou for help on the CT25 analysis. The work of MG is partially supported by the National Science Foundation under Grant No. PHY-2412071. KM was supported in part by the US National Science Foundation under Grant PHY-2310497. PMN and SD are grateful for support from the Wu-Ki Tung Endowed Chair in particle physics. The work of SD was also supported by the National Natural Science Foundation of China under

Grant number 12475079. The work of CPY is supported by the U.S. National Science Foundation under Grant No. PHY-2310291.

Appendix A: New LHC data sets included in the CT25 NNLO analysis

In this appendix, we provide additional details on the newly included data sets listed in Table I of the main narrative.

Lepton pair production measurements. As in the CT18A global fit, we include the precision measurement of W and Z production by ATLAS collaboration at 7 TeV [29]. This measurement revealed an enhancement in the strangeness PDF at $x \sim 0.02$ – a trend that was corroborated by more recent observations at the LHC. In Ref. [26], we examined in depth the implications of these measurements for PDFs and identified the following differential cross sections for inclusion in the final CT25 fit:

1. From the ATLAS collaboration:

- (a) muon pseudorapidity distribution in W boson production ($W \rightarrow \mu\nu$) at a center-of-mass energy $\sqrt{s} = 8$ TeV [40] with 20.2 fb^{-1} of integrated luminosity (IL), in fiducial volume $p_T^{l,\nu} > 25$ GeV, $|\eta_\mu| < 2.4$, $m_T > 40$ GeV;
- (b) W^\pm muon pseudorapidity and Z dilepton rapidity distributions [43] in $\sqrt{s} = 5.02$ TeV with 25 pb^{-1} of IL, in the fiducial phase space $p_T^{l,\nu} > 25$ GeV, $|\eta_l| < 2.5$, $m_T > 40$ GeV for W^\pm bosons and $p_T^l > 20$ GeV, $|\eta_l| < 2.5$, $66 < m_{ll} < 116$ GeV for Z bosons;
- (c) triple differential distribution in Z boson production in electron and muon decay channels [42], presented in terms of invariant mass m_{ll} , rapidity of dilepton pair y_{ll} , and cosine of the polar angle in the Collins-Soper frame, with an IL of 35.9 fb^{-1} , $p_T^l > 20$ GeV, $|\eta_l| < 2.4$, $46 < m_{ll} < 200$ GeV.

2. From the CMS collaboration:

rapidity distribution for Z boson production at 13 TeV [41] with an IL of 35.9 fb^{-1} , $p_T^l > 20$ GeV, $|\eta_l| < 2.4$ and $|m_{ll} - M_Z| < 15$ GeV.

3. From the LHCb collaboration:

- (a) electron pseudorapidity differential cross section in $W \rightarrow e\nu$ production [44] at $\sqrt{s} = 8$ TeV with an IL of 2 fb^{-1} , $2.0 < \eta < 4.25$ and $p_T^e > 20$ GeV;
- (b) dilepton rapidity distribution in Z boson production in electron and muon decay channels at $\sqrt{s} = 13$ TeV [45] with 0.29 fb^{-1} of IL, $2.0 < \eta_l < 4.5$, $p_T^l > 20$ GeV, $60 < m_{ll} < 120$ GeV.

Top-quark pair production measurements. For top-quark pair production, we included the following measurements at $\sqrt{s} = 13$ TeV based on the study of their impact on post-CT18 PDFs in Ref. [27]:

1. From the ATLAS collaboration:
 - (a) rapidity distribution of the $t\bar{t}$ pair, $d\sigma/dy_{t\bar{t}}$, in the all-hadronic channel [53] with an IL of 36.1 fb⁻¹ in the full phase space at parton level;
 - (b) the statistically combined $m_{t\bar{t}} + y_{t\bar{t}} + y_{t\bar{t}}^B + H_T^{t\bar{t}}$ distributions [56], with 36 fb⁻¹ of IL, where $y_{t\bar{t}}^B$ denotes the reconstructed rapidity of the $t\bar{t}$ system in the boosted topology, and $H_T^{t\bar{t}}$ is the scalar sum of the transverse momenta of the hadronic and leptonic top quarks, $H_T^{t\bar{t}} = p_t^{had} + p_{\bar{t}}^{lep}$.
2. From the CMS collaboration:
 - (a) the $y_{t\bar{t}}$ distribution in the dilepton channel [54] with 35.9 fb⁻¹ of IL;
 - (b) the $m_{t\bar{t}}$ distribution in the lepton+jet channel [55] with 137 fb⁻¹ of IL.

Single-inclusive jet production measurements. In Ref. [28], we compared constraints imposed on our post-CT18 PDFs by the latest LHC cross sections in hadronic jet production. While these cross sections can be included in the form of either inclusive single-jet or jet-pair distributions, Ref. [28] found it preferable to fit the single-inclusive jet cross sections only, in light of the stronger dependence of theory predictions in dijet production on the choice of renormalization and factorization scales. Based on the detailed examination of candidate jet cross sections in Ref. [28], the CT25 analysis includes the following single-inclusive jet production data sets:

1. From the ATLAS collaboration:
 - (a) the $d^2\sigma/(dp_T d|y|)$ distribution at $\sqrt{s} = 8$ TeV [46] with 20.2 fb⁻¹ of IL, jet radius $R = 0.6$, in the fiducial volume $|y| < 3$ and $70 \leq p_T^{jet} \leq 2500$ GeV;
 - (b) the $d^2\sigma/(dp_T d|y|)$ distribution at $\sqrt{s} = 13$ TeV [47] with 3.2 fb⁻¹ of IL, $R = 0.4$, $|y| < 3$ and $100 \leq p_T^{jet} \leq 3937$ GeV.
2. From the CMS collaboration,
 - (a) In the CT25prel fit, we include $d^2\sigma/dp_T d|y|$ distributions at $\sqrt{s} = 13$ TeV [52] with 33.5 fb⁻¹ of IL, $R = 0.7$, $|y| < 2$ and $97 \leq p_T^{jet} \leq 3103$ GeV.

- (b) In the CT25 fit, we include $d^2\sigma/(dp_T dy)$ distributions at $\sqrt{s} = 7$ TeV with an IL of 5 fb^{-1} (ID=556) [6, 49–51], at $\sqrt{s} = 8$ TeV with an IL of 19.7 fb^{-1} (ID=557) [6, 52], and at $\sqrt{s} = 13$ TeV with an IL of 33.5 fb^{-1} (ID=555) [6, 48]. The 7 TeV measurements include 118 data points in six rapidity bins covering $0 \leq |y| \leq 2.5$, with jet transverse momenta in the range $114 \leq p_T \leq 1327$ GeV. The 8 TeV measurements include 164 data points in six rapidity bins covering $0 \leq |y| \leq 3.0$, with $74 \leq p_T \leq 1784$ GeV. The 13 TeV measurements include 78 data points, $|y| < 2$ and $97 \leq p_T^{jet} \leq 3103$ GeV. These CMS 7, 8, 13 TeV measurements have updated systematic uncertainties and newly provided statistical correlation matrices [6, 51]. They supersede the earlier inclusive-jet datasets at 7 TeV (ID=542) [49, 50], 8 TeV (ID=545) [52], and 13 TeV (ID=555) [48] included in previous analyses [16, 28].

Appendix B: Investigation of reclustering prescriptions

In continuation of the discussion in Sec. IV.6.1, we illustrate the possibility of separate reclustering of the residuals and nuisance parameters by two figures. Figure 12 goes back to the example of the GT and DT uncertainties for the published data sets in Fig. 6 for the CT25 baseline and now shows the DT uncertainties constructed only with D^2 and only with R^2 for the CT25prel baseline.⁹ The GT and DT uncertainties based only on residuals (i.e., without R^2) are wider than the corresponding ones based on both residuals and nuisance parameters ($D^2 + R^2$). The role of R^2 appears to be somewhat different for the GT and DT cases. In the DT case, the R^2 has a more constraining power on the uncertainty: if it were to be the only metric for the uncertainty, we would obtain a very small error (blue dashed band). However, R^2 is in general not perfectly determined, due to lack of full control on the correlated systematic uncertainties. The R^2 effect is less pronounced for the GT.

Figure 8 showed how the 68% and 90% CL error estimates change when we vary the DT clustering procedure. Figure 13 extends this comparison to show error estimates for other credibility levels, including the residuals only (that is, neglecting R^2). In this figure, the “Global T: no R^2 ” and “Dynamical T: no R^2 ” refer to the GT and DT uncertainties based on the full baseline. The “52 alt. clusters” and other lines refer to randomly generated clusters constructed by reshuffling the residuals in the 52 experimental data sets of CT25prel. For the alternative clusters, the lines show the envelopes of the DT estimates for 200 shuffles of the corresponding alternative clusters. In an ideal scenario, in the absence of tensions among the data, alternative cluster configurations would produce approximately the same estimate for the $\alpha_s(M_Z)$ uncertainty. In reality, when we partition into a lot of clusters, taking the outcome of the

⁹ These uncertainties do not change much between the two baselines. In this and following figure, the lower bands saturate at $\alpha_s(M_Z) = 0.113$, the lowest point on our α_s grid.

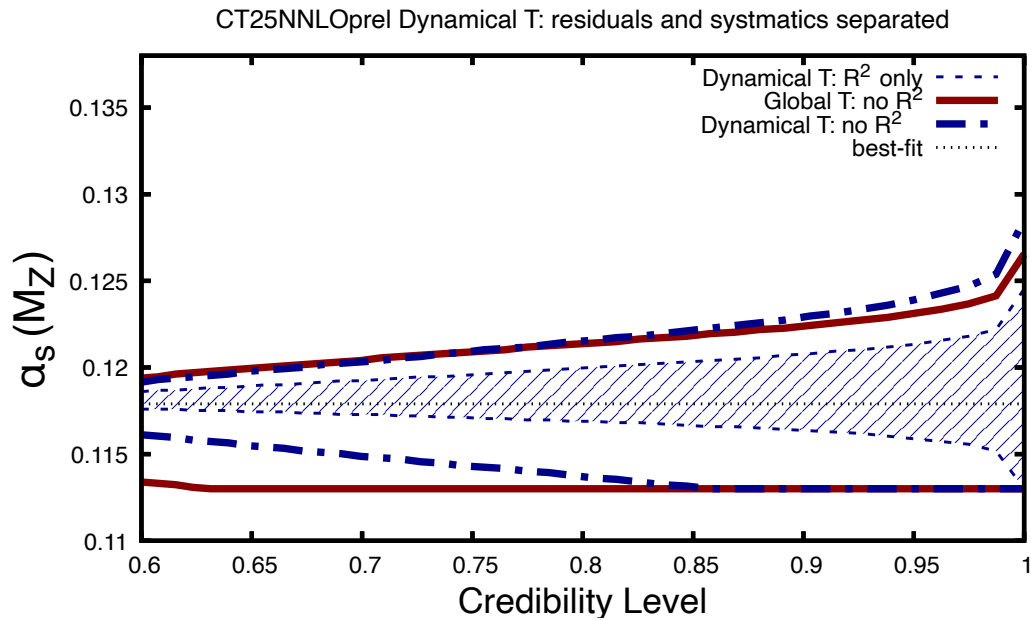


FIG. 12. Contributions to the GT and DT uncertainties vs. the credibility level for the CT25prel baseline from nuisance parameters (R^2) only and from residuals (D^2) without R^2 .

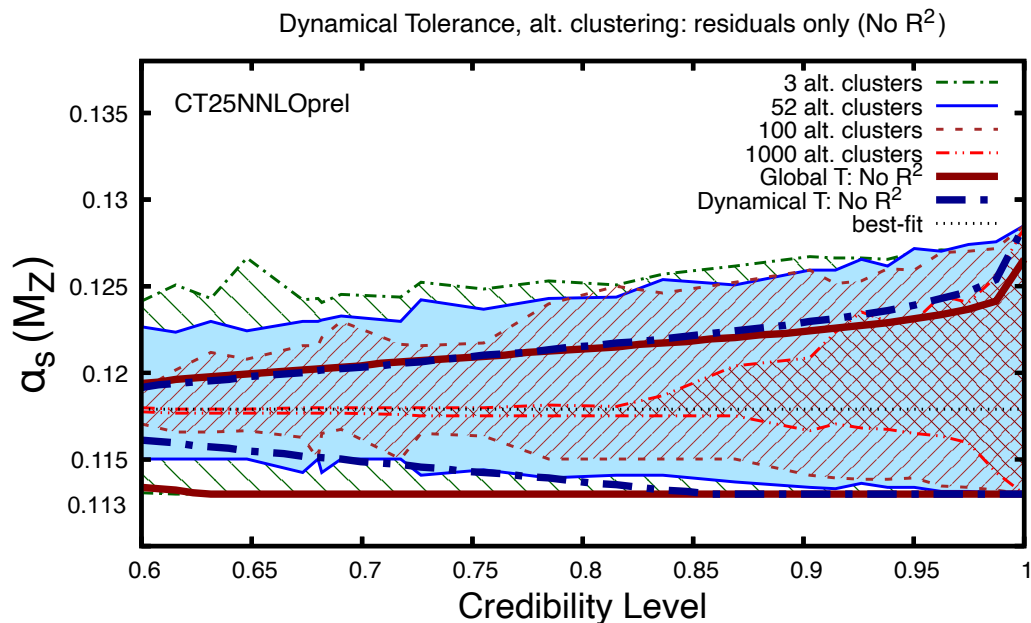


FIG. 13. Reclustering without R^2 : $\alpha_s(M_Z)$ as a function of the credibility level for the dynamical and global tolerance criteria compared to different alternative cluster configurations.

DT without R^2 by itself may already produce a stringent (likely, too stringent) uncertainty on $\alpha_s(M_Z)$. However, the constraints may be weaker for other cluster configurations, and including R^2 into clustering may additionally reduce or increase the strength of the DT constraints by modifying the tensions, similarly to what we saw for the DT that reclustered the published data sets.

Appendix C: A toy example of uncertainty under K-folding

This appendix provides details about the toy study of K-folding summarized in Sec. IV.6.2. Working with the best-fit residuals and nuisance parameters (assumed to be mutually independent) in the setup of Sec. IV.6, we divide the baseline data into four clusters according to randomly generated partitions (“configurations”). In contrast to the full K-folding procedure, we will not refit (optimize) the PDFs for each configuration, which would be too computationally expensive. Instead, we examine uncertainties by reclustering the output of the CT25prel global fit, similarly to what was done in the previous sections. In addition, to assess their independent impact, we will separately consider the residual and nuisance-parameter contributions.

Dependence of the central $\alpha_s(M_Z)$ on clustering. We generate multiple partitions of the residuals from \mathbf{v}_r into four clusters, with about 1113 points in each cluster, as outlined in Sec. IV.6.1. Table IV reports the numbers of points and χ^2 contributions for three representative configurations in our series. Similarly, we construct four “ R^2 ” clusters consisting of the shuffled best-fit nuisance parameters from \mathbf{v}_λ . Figure 9 illustrates the outcome of one such exercise, in which 100 configurations of four clusters were generated. The figure separately depicts the individual χ^2/N_{pt} ratios for the residuals (purple lines) and nuisance parameters (red-dashed lines). Each purple (red) line corresponds to a different configuration. The black lines represent the χ^2/N_{pt} average values. The stars represent the minima of the average curves which indicate the $\alpha_s(M_Z)$ central-value preference. No tolerance criterion is applied here; we simply calculate the χ^2/N_{pt} for each configuration at different $\alpha_s(M_Z)$.

	cluster 0	cluster 1	cluster 2	cluster 3
N_{pt}	1113	1113	1112	1112
	χ^2_R (no R^2)			
configuration 1	1094	1157	1281	1177
configuration 2	1102	1158	1252	1198
configuration 3	1065	1239	1251	1156

TABLE IV. Numbers of points and χ^2_R (without the systematic contribution R^2) for three random partitions (configurations) of the residuals into four pseudodata clusters.

One goal of this exercise is to determine whether the random fluctuations due to the reshuffling process are compatible with their $\mathcal{N}(0, 1)$ distribution expected when the data sets mutually agree. The χ^2/N_{pt} vs. $\alpha_s(M_Z)$ for the latter case is shown in Fig. 10, for which we generated an ensemble of the “cluster 0” configurations from pseudoresiduals that were generated according to $\mathcal{N}(0, 1)$ from a baseline pseudodata without tensions and assuming the “truth” $\alpha_s(M_Z) = 0.119$.

It is therefore interesting to confront the idealized pseudoresidual scenario against the realistic distributions of the residual and R^2 clusters. In the ideal case in Fig. 10, the clusters follow a deep parabola centered at the “truth” $\alpha_s(M_Z)$. In the real case in Fig. 9, all clusters have shallower dependence on $\alpha_s(M_Z)$. The parabolic behavior is particularly wide for the residuals and slightly narrower for the nuisance parameters. The clusters of the real residuals all prefer an approximately stable value of $\alpha_s(M_Z) \approx 0.1165$. The preferred $\alpha_s(M_Z)$ of the R^2 clusters varies more, between 0.119 and 0.121 depending on the cluster. We read off these values from the central curves of each cluster, obtained by averaging the χ^2/N_{pt} curves over many alternative configurations. The fluctuations around these curves, however, are roughly of the same magnitude as in the idealized case of Fig. 10. These observations suggest that tensions among the data sets primarily flatten the χ^2/N_{pt} curves relatively to the no-tension scenario. They also introduce variability in the preferred values of $\alpha_s(M_Z)$ for the R^2 clusters, as different groups of experimental systematic uncertainties exert substantial and inconsistent pulls on $\alpha_s(M_Z)$.

$\alpha_s(M_Z)$ **uncertainty in the four-cluster exercise.** Figure 9 demonstrates that the χ^2/N_{pt} dependence of clusters is shallower than in the idealized case for which the $\Delta\chi^2 = 1$ prescription is applicable. The question arises how to quantify the uncertainty in this situation. As was already stated, in an NNPDF-like approach, the α_s uncertainties from individual iterations would affect the weights for the final α_s averaging, and the final outcome would also reflect refitting the PDFs for each data partition into clusters, as well as averaging over partitions’ sizes, which is beyond the scope of this study.

Just as one possibility, if the DT criterion is applied either to the “training set” consisting of 3 clusters or 1 “testing” cluster, it can render the uncertainty that can be substantially larger or smaller than the $^{+0.0007}_{-0.0014}$ from the NNPDF study. In its most granular realization, the DT criterion treats each residual as an independent “experiment”. Table V summarizes the outcome of applying such DT criterion to the three training clusters of the residuals (no R^2) and to the one left out. Here we show the DT α_s uncertainties for the same three configurations as in Table IV. These uncertainties can be either substantially smaller or larger than the NNPDF one, depending on the specific partition. The table also highlights the observation that, within a combination of any three clusters, the DT uncertainty of the whole cluster is equal to the smallest individual DT uncertainty among the constituent clusters. For this specific example, cluster 0 has the lowest χ^2 for the three configurations, cf. Table IV. When combined with the other two, this cluster

configuration 1

$\delta\alpha_s(M_Z) =$	+0.00180 -0.00062	+0.00230 -0.00400	+0.00410 -0.00490	+0.00830 -0.00490
in 1-clusters:	{0}	{1}	{3}	{2}
& 3-clusters:	{0,1,2}, {0,1,3}, {0,2,3}	{1,2,3}	N/A	N/A

configuration 2

$\delta\alpha_s(M_Z) =$	+0.00102 -0.00038	+0.00507 -0.00490	+0.00515 -0.00490	+0.00943 -0.00490
in 1-clusters:	{0}	{1}	{3}	{2}
& 3-clusters:	{0,1,2}, {0,1,3}, {0,2,3}	{1,2,3}	N/A	N/A

configuration 3

$\delta\alpha_s(M_Z) =$	+0.00016 -0.00038	+0.00480 -0.00290	+0.00803 -0.00490	+0.00819 -0.00490
in 1-clusters:	{0}	{3}	{1}	{2}
& 3-clusters:	{0,1,2}, {0,1,3}, {0,2,3}	{1,2,3}	N/A	N/A

TABLE V. For each configuration of the K-folding exercise, we report the $\delta\alpha_s$ values found by applying the DT, as well as the one 1-cluster and three 3-clusters for which these $\delta\alpha_s$ are achieved. The columns containing the $\delta\alpha_s$ values and clusters are arranged so that the leftmost (rightmost) column contains the lowest (highest) $\delta\alpha_s$.

drives the net uncertainty of the combination. For the fourth 3-cluster combination, the uncertainty is set by the second most precise individual cluster. According to the findings in Table V, the uncertainty on $\alpha_s(M_Z)$ is not uniformly reproduced by each test cluster, and this is mainly ascribed to the tensions in the data. The results do not change if we consider the average of the errors over a large number of configurations.

Appendix D: Information Criteria and the GMM

We use the Akaike Information Criterion (AIC) to determine the optimal number of Gaussian mixtures K for the GMM. The AIC score is defined as

$$\text{AIC} = N_p \ln N_{\text{pt}} - 2 \ln L(\bar{\alpha}_s) \quad (\text{D1})$$

where $L(\bar{\alpha}_s)$ is the GMM likelihood given in Eq. (5.4) evaluated at the optimized value of α_s , N_{pt} is the number of data clusters, and the number of independent parameters N_p for the GMM is given by

$$N_p = K \times N_{\text{par}} + (K - 1). \quad (\text{D2})$$

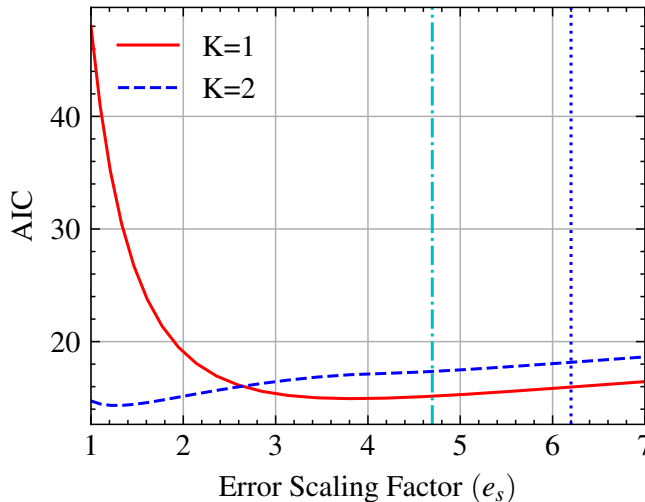


FIG. 14. Variation of the AIC score with the error scaling factor e_S shown for both $K = 1$ (red) and $K = 2$ (blue) in the GMM. Also shown are the values of $e_{SPDG} \approx 4.7$ (dot-dashed) and $e_{SGMM} \approx 6.2$ (dotted) – see the discussion in Sec. V.2.

Since we profile the χ^2 over $\alpha_s(M_Z)$, $N_{\text{par}} = 1$. We vary the value of K from 1 through 5 and find that the value of K that minimizes the AIC score is $K = 2$. Our GMM result in Eq. (5.5) quotes the α_s value for $K = 2$.

This result is obtained for the actual input errors corresponding to error scaling factor $e_S = 1$. In Fig. 14, we further illustrate how inflating the input uncertainties could modify the AIC analysis by plotting the AIC score vs. e_S for two models: the usual $\sum_i \chi^2(\bar{\alpha}_s, \alpha_{s,i}, \sigma_i)$ in Sec. IV.2, which corresponds to the choice $K = 1$, and the GMM with $K = 2$. The $K = 2$ case achieves the lowest overall AIC score at $e_S \approx 1.2$, close to the nominal $e_S = 1$.

For $e_S = 1$, the $K = 2$ model returns a weighted average of two distinct values of $\alpha_s(M_Z) = \{0.1154, 0.1193\}$. As e_S increases, the data become more consistent, thus increasing the AIC score for $K = 2$ and reducing it for $K = 1$. Beyond the value of $e_S \approx 2.6$, the $K = 1$ model would be a preferred choice. For $e_S \approx 2.6$, the fit is still of poor quality with a large $\sum_i \chi^2(\bar{\alpha}_s, \alpha_{s,i}, \sigma_i)$, hence we do not use this as a measure to set the value of e_S for $K = 1$. For values of $e_S \gtrsim 3.5$, the AIC curves for both models grow linearly with the same slope. For these values of e_S , the $K = 2$ model does not find two numerically distinct values of $\alpha_s(M_Z)$ and therefore behaves like the $K = 1$ model, albeit with some overfitting due to its larger number of parameters. This also explains a dip in the uncertainty for $K = 2$ at $e_S \approx 4.2$ in Fig. 11, above which the $K = 2$ uncertainty starts to track that for $K = 1$. The slightly larger AIC score and uncertainties for $K = 2$ for $e_S \gtrsim 3.5$ arise due to overfitting [86].

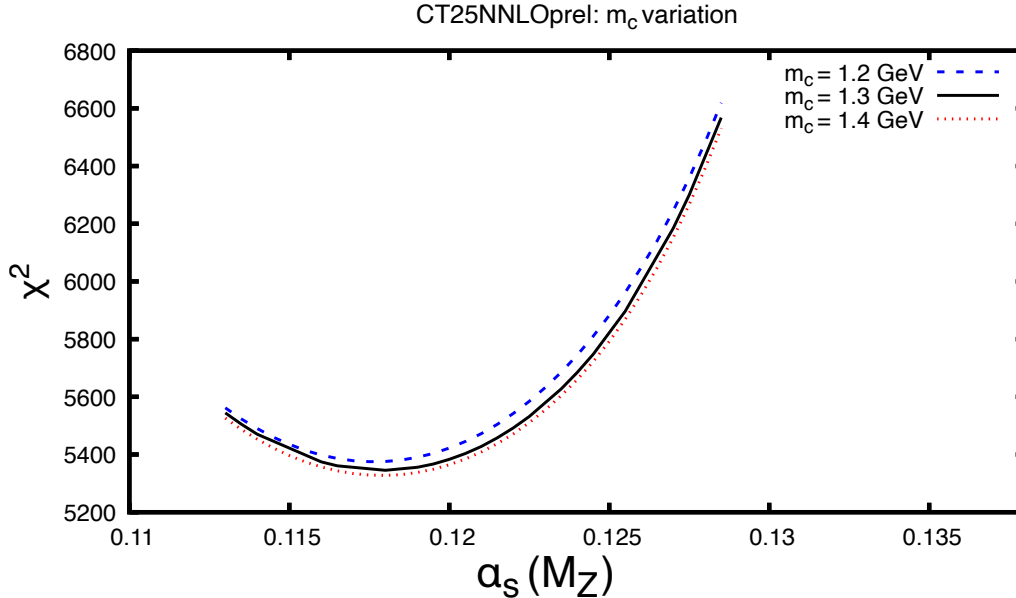


FIG. 15. χ^2 as a function of $\alpha_s(M_Z)$ in correspondence of the three values of m_c considered in this analysis.

Appendix E: Sensitivity to charm-quark mass variations

To investigate the sensitivity of the results to the charm-quark pole mass m_c , we extracted $\alpha_s(M_Z)$ from two additional χ^2_R scans obtained with $m_c = 1.2$ GeV and $m_c = 1.4$ GeV respectively. The default charm-quark mass value used in the CT25 global analysis is $m_c = 1.3$ GeV.

From the global tolerance criterion, we obtain the following results with the CT25prel baseline:

$$\alpha_s(M_Z) = 0.1175^{+0.0025}_{-0.0023}, \quad m_c = 1.2 \text{ GeV}; \quad (\text{E1})$$

$$\alpha_s(M_Z) = 0.1179^{+0.0024}_{-0.0025}, \quad m_c = 1.3 \text{ GeV}; \quad (\text{E2})$$

$$\alpha_s(M_Z) = 0.1179^{+0.0024}_{-0.0025}, \quad m_c = 1.4 \text{ GeV}. \quad (\text{E3})$$

From this we note that the impact on the uncertainty is negligible, which is also reflected in Figure 15 showing the global χ^2 as a function of $\alpha_s(M_Z)$ for the three values of m_c .

With the dynamical tolerance criterion we obtain at 68% CL:

$$\alpha_s(M_Z) = 0.1175^{+0.0019}_{-0.0011}, \quad m_c = 1.2 \text{ GeV}; \quad (\text{E4})$$

$$\alpha_s(M_Z) = 0.1179^{+0.0024}_{-0.0012}, \quad m_c = 1.3 \text{ GeV}; \quad (\text{E5})$$

$$\alpha_s(M_Z) = 0.1179^{+0.0025}_{-0.0013}, \quad m_c = 1.4 \text{ GeV}. \quad (\text{E6})$$

The DT errors from alternative clustering for the different m_c values behave similarly to those discussed in Sec. IV.

-
- [1] D. d’Enterria *et al.*, *The strong coupling constant: state of the art and the decade ahead*, *J. Phys. G* **51**, 090501 (2024), [arXiv:2203.08271 \[hep-ph\]](#).
- [2] G. P. Salam, The strong coupling: a theoretical perspective, in *From My Vast Repertoire ...: Guido Altarelli’s Legacy*, edited by A. Levy, S. Forte, and G. Ridolfi (2019) pp. 101–121, [arXiv:1712.05165 \[hep-ph\]](#).
- [3] F. Dulat, A. Lazopoulos, and B. Mistlberger, *iHixs 2 — Inclusive Higgs cross sections*, *Comput. Phys. Commun.* **233**, 243–260 (2018), [arXiv:1802.00827 \[hep-ph\]](#).
- [4] S. Navas *et al.* (Particle Data Group Collaboration), *Review of particle physics*, *Phys. Rev. D* **110**, 030001 (2024).
- [5] G. Aad *et al.* (ATLAS), A precise determination of the strong-coupling constant from the recoil of Z bosons with the ATLAS experiment at $\sqrt{s} = 8$ TeV (2023), [arXiv:2309.12986 \[hep-ex\]](#).
- [6] V. Chekhovsky *et al.* (CMS), *Determination of the strong coupling and its running from measurements of inclusive jet production*, *Phys. Lett. B* **868**, 139651 (2025), [arXiv:2412.16665 \[hep-ex\]](#).
- [7] A. Hayrapetyan *et al.* (CMS), *Measurement of multijet azimuthal correlations and determination of the strong coupling in proton-proton collisions at $\sqrt{s} = 13$ TeV*, *Eur. Phys. J. C* **84**, 842 (2024), [arXiv:2404.16082 \[hep-ex\]](#).
- [8] A. Hayrapetyan *et al.* (CMS), *Measurement of Energy Correlators inside Jets and Determination of the Strong Coupling $\alpha_S(m_Z)$* , *Phys. Rev. Lett.* **133**, 071903 (2024), [arXiv:2402.13864 \[hep-ex\]](#).
- [9] G. Aad *et al.* (ATLAS), *Determination of the strong coupling constant from transverse energy–energy correlations in multijet events at $\sqrt{s} = 13$ TeV with the ATLAS detector*, *JHEP* **07**, 085, [arXiv:2301.09351 \[hep-ex\]](#).
- [10] V. Andreev *et al.* (H1), *Determination of the strong coupling constant $\alpha_s(m_Z)$ in next-to-next-to-leading order QCD using H1 jet cross section measurements*, *Eur. Phys. J. C* **77**, 791 (2017), [Erratum: *Eur.Phys.J.C* 81, 738 (2021)], [arXiv:1709.07251 \[hep-ex\]](#).
- [11] Y. Aoki *et al.* (Flavour Lattice Averaging Group (FLAG)), *FLAG Review 2024* (2024), [arXiv:2411.04268 \[hep-lat\]](#).
- [12] National Academies of Sciences, Engineering, and Medicine, *Reproducibility and Replicability in Science* (The National Academies Press, Washington, DC, 2019).
- [13] P. J. Mohr, D. B. Newell, B. N. Taylor, and E. Tiesinga, *Codata recommended values of the fundamental physical constants: 2022*, *Rev. Mod. Phys.* **97**, 025002 (2025).
- [14] In preparation (2025).
- [15] H.-L. Lai, J. Huston, Z. Li, P. Nadolsky, J. Pumplin, D. Stump, and C. P. Yuan, *Uncertainty induced by QCD coupling in the CTEQ global analysis of parton distributions*, *Phys. Rev.* **D82**, 054021 (2010), [arXiv:1004.4624 \[hep-ph\]](#).
- [16] T.-J. Hou *et al.*, *New CTEQ global analysis of quantum chromodynamics with high-precision data from the LHC*, *Phys. Rev. D* **103**, 014013 (2021), [arXiv:1912.10053 \[hep-ph\]](#).
- [17] S. Alekhin, J. Blümlein, S. Moch, and R. Placakyte, *Parton distribution functions, α_s , and heavy-quark masses for LHC Run II*, *Phys. Rev.* **D96**, 014011 (2017), [arXiv:1701.05838 \[hep-ph\]](#).
- [18] A. Gizhko *et al.*, *Running of the Charm-Quark Mass from HERA Deep-Inelastic Scattering Data*, *Phys. Lett.*

- B 775**, 233–238 (2017), [arXiv:1705.08863 \[hep-ph\]](#).
- [19] R. D. Ball, S. Carrazza, L. Del Debbio, S. Forte, Z. Kassabov, J. Rojo, E. Slade, and M. Ubiali (NNPDF), *Precision determination of the strong coupling constant within a global PDF analysis*, *Eur. Phys. J. C* **78**, 408 (2018), [arXiv:1802.03398 \[hep-ph\]](#).
- [20] T. Cridge, L. A. Harland-Lang, A. D. Martin, and R. S. Thorne, *An investigation of the α_S and heavy quark mass dependence in the MSHT20 global PDF analysis*, *Eur. Phys. J. C* **81**, 744 (2021), [arXiv:2106.10289 \[hep-ph\]](#).
- [21] T. Cridge and M. A. Lim, *Constraining the top-quark mass within the global MSHT PDF fit*, *Eur. Phys. J. C* **83**, 805 (2023), [arXiv:2306.14885 \[hep-ph\]](#).
- [22] S. Alekhin, M. V. Garzelli, S. O. Moch, and O. Zenaiev, *NNLO PDFs driven by top-quark data*, *Eur. Phys. J. C* **85**, 162 (2025), [arXiv:2407.00545 \[hep-ph\]](#).
- [23] T. Cridge, L. A. Harland-Lang, and R. S. Thorne, *A first determination of the strong coupling α_S at approximate N^3LO order in a global PDF fit*, *Eur. Phys. J. C* **84**, 1009 (2024), [arXiv:2404.02964 \[hep-ph\]](#).
- [24] R. D. Ball, A. Barontini, J. Cruz-Martinez, S. Forte, F. Hekhorn, E. R. Nocera, J. Rojo, and R. Stegeman (NNPDF), *A Determination of $\alpha_s(M_Z)$ at $aN^3LO_{\text{QCD}} \otimes \text{NLO}_{\text{QED}}$ Accuracy from a Global PDF Analysis*, *Eur. Phys. J. C* **85**, 1001 (2025), [arXiv:2506.13871 \[hep-ph\]](#).
- [25] K. Kovařík, P. M. Nadolsky, and D. E. Soper, *Hadronic structure in high-energy collisions*, *Rev. Mod. Phys.* **92**, 045003 (2020), [arXiv:1905.06957 \[hep-ph\]](#).
- [26] I. Sitiwaldi, K. Xie, A. Ablat, S. Dulat, T.-J. Hou, and C. P. Yuan (CTEQ-TEA), *Precision studies of the post-CT18 LHC Drell-Yan data in the CTEQ-TEA global analysis*, *Phys. Rev. D* **108**, 034030 (2023), [arXiv:2305.10733 \[hep-ph\]](#).
- [27] A. Ablat, M. Guzzi, K. Xie, S. Dulat, T.-J. Hou, I. Sitiwaldi, and C. P. Yuan, *Exploring the impact of high-precision top-quark pair production data on the structure of the proton at the LHC*, *Phys. Rev. D* **109**, 054027 (2024), [arXiv:2307.11153 \[hep-ph\]](#).
- [28] A. Ablat, S. Dulat, T.-J. Hou, J. Huston, P. Nadolsky, I. Sitiwaldi, K. Xie, and C. P. Yuan (CTEQ-TEA), *Impact of LHC precision measurements of inclusive jet and dijet production on the CTEQ-TEA global PDF fit*, *Phys. Rev. D* **111**, 036033 (2025), [arXiv:2412.00350 \[hep-ph\]](#).
- [29] M. Aaboud *et al.* (ATLAS), *Precision measurement and interpretation of inclusive W^+ , W^- and Z/γ^* production cross sections with the ATLAS detector*, *Eur. Phys. J. C* **77**, 367 (2017), [arXiv:1612.03016 \[hep-ex\]](#).
- [30] H. Abramowicz *et al.* (ZEUS, H1), *Combination and QCD Analysis of Charm Production Cross Section Measurements in Deep-Inelastic ep Scattering at HERA*, *Eur. Phys. J. C* **73**, 2311 (2013), [arXiv:1211.1182 \[hep-ex\]](#).
- [31] A. Aktas *et al.* (H1), *Measurement of $F_2(c\bar{c})$ and $F_2(b\bar{b})$ at high Q^2 using the H1 vertex detector at HERA*, *Eur. Phys. J. C* **40**, 349–359 (2005), [arXiv:hep-ex/0411046 \[hep-ex\]](#).
- [32] H. Abramowicz *et al.* (H1, ZEUS), *Combination and QCD analysis of charm and beauty production cross-section measurements in deep inelastic ep scattering at HERA*, *Eur. Phys. J. C* **78**, 473 (2018), [arXiv:1804.01019 \[hep-ex\]](#).
- [33] J. Dove *et al.* (SeaQuest), *The asymmetry of antimatter in the proton*, *Nature* **590**, 561–565 (2021), [Erratum:

- Nature 604, E26 (2022)], [arXiv:2103.04024 \[hep-ph\]](#).
- [34] J. P. Berge *et al.*, *A Measurement of Differential Cross-Sections and Nucleon Structure Functions in Charged Current Neutrino Interactions on Iron*, *Z. Phys.* **C49**, 187–224 (1991).
- [35] U.-K. Yang *et al.* (CCFR/NuTeV), *Measurements of F_2 and $xF_3^{\nu} - xF_3^{\bar{\nu}}$ from CCFR ν_{μ} -Fe and $\bar{\nu}_{\mu}$ -Fe data in a physics model independent way*, *Phys. Rev. Lett.* **86**, 2742–2745 (2001), [arXiv:hep-ex/0009041 \[hep-ex\]](#).
- [36] W. G. Seligman *et al.*, *Improved determination of $\alpha(s)$ from neutrino nucleon scattering*, *Phys. Rev. Lett.* **79**, 1213–1216 (1997), [arXiv:hep-ex/9701017 \[hep-ex\]](#).
- [37] E. Rondio (NMC), *Nuclear effects in deep inelastic scattering*, *Nucl. Phys. A* **553**, 615C–624C (1993).
- [38] F. D. Aaron *et al.* (H1), *Measurement of the Inclusive e -pmp Scattering Cross Section at High Inelasticity y and of the Structure Function F_L* , *Eur. Phys. J. C* **71**, 1579 (2011), [arXiv:1012.4355 \[hep-ex\]](#).
- [39] H.-L. Lai, M. Guzzi, J. Huston, Z. Li, P. M. Nadolsky, J. Pumplin, and C. P. Yuan, *New parton distributions for collider physics*, *Phys. Rev.* **D82**, 074024 (2010), [arXiv:1007.2241 \[hep-ph\]](#).
- [40] G. Aad *et al.* (ATLAS), *Measurement of the cross-section and charge asymmetry of W bosons produced in proton-proton collisions at $\sqrt{s} = 8$ TeV with the ATLAS detector*, *Eur. Phys. J. C* **79**, 760 (2019), [arXiv:1904.05631 \[hep-ex\]](#).
- [41] A. M. Sirunyan *et al.* (CMS), *Measurements of differential Z boson production cross sections in proton-proton collisions at $\sqrt{s} = 13$ TeV*, *JHEP* **12**, 061, [arXiv:1909.04133 \[hep-ex\]](#).
- [42] M. Aaboud *et al.* (ATLAS), *Measurement of the Drell-Yan triple-differential cross section in pp collisions at $\sqrt{s} = 8$ TeV*, *JHEP* **12**, 059, [arXiv:1710.05167 \[hep-ex\]](#).
- [43] M. Aaboud *et al.* (ATLAS), *Measurements of W and Z boson production in pp collisions at $\sqrt{s} = 5.02$ TeV with the ATLAS detector*, *Eur. Phys. J. C* **79**, 128 (2019), [Erratum: *Eur.Phys.J.C* 79, 374 (2019)], [arXiv:1810.08424 \[hep-ex\]](#).
- [44] R. Aaij *et al.* (LHCb), *Measurement of forward $W \rightarrow e\nu$ production in pp collisions at $\sqrt{s} = 8$ TeV*, *JHEP* **10**, 030, [arXiv:1608.01484 \[hep-ex\]](#).
- [45] R. Aaij *et al.* (LHCb), *Precision measurement of forward Z boson production in proton-proton collisions at $\sqrt{s} = 13$ TeV*, *JHEP* **07**, 026, [arXiv:2112.07458 \[hep-ex\]](#).
- [46] M. Aaboud *et al.* (ATLAS), *Measurement of the inclusive jet cross-sections in proton-proton collisions at $\sqrt{s} = 8$ TeV with the ATLAS detector*, *JHEP* **09**, 020, [arXiv:1706.03192 \[hep-ex\]](#).
- [47] M. Aaboud *et al.* (ATLAS), *Measurement of inclusive jet and dijet cross-sections in proton-proton collisions at $\sqrt{s} = 13$ TeV with the ATLAS detector*, *JHEP* **05**, 195, [arXiv:1711.02692 \[hep-ex\]](#).
- [48] A. Tumasyan *et al.* (CMS), *Measurement and QCD analysis of double-differential inclusive jet cross sections in proton-proton collisions at $\sqrt{s} = 13$ TeV*, *JHEP* **02**, 142, [Addendum: *JHEP* 12, 035 (2022)], [arXiv:2111.10431 \[hep-ex\]](#).
- [49] S. Chatrchyan *et al.* (CMS), *Measurements of Differential Jet Cross Sections in Proton-Proton Collisions at $\sqrt{s} = 7$ TeV with the CMS Detector*, *Phys. Rev. D* **87**, 112002 (2013), [Erratum: *Phys.Rev.D* 87, 119902 (2013)], [arXiv:1212.6660 \[hep-ex\]](#).
- [50] S. Chatrchyan *et al.* (CMS), *Measurement of the Ratio of Inclusive Jet Cross Sections using the Anti- k_T Algorithm with Radius Parameters $R=0.5$ and 0.7 in pp Collisions at $\sqrt{s} = 7$ TeV*, *Phys. Rev. D* **90**, 072006

- (2014), [arXiv:1406.0324 \[hep-ex\]](#).
- [51] V. Khachatryan *et al.* (CMS), *Constraints on parton distribution functions and extraction of the strong coupling constant from the inclusive jet cross section in pp collisions at $\sqrt{s} = 7$ TeV*, *Eur. Phys. J. C* **75**, 288 (2015), [arXiv:1410.6765 \[hep-ex\]](#).
- [52] V. Khachatryan *et al.* (CMS), *Measurement and QCD analysis of double-differential inclusive jet cross sections in pp collisions at $\sqrt{s} = 8$ TeV and cross section ratios to 2.76 and 7 TeV*, *JHEP* **03**, 156, [arXiv:1609.05331 \[hep-ex\]](#).
- [53] G. Aad *et al.* (ATLAS), *Measurements of top-quark pair single- and double-differential cross-sections in the all-hadronic channel in pp collisions at $\sqrt{s} = 13$ TeV using the ATLAS detector*, *JHEP* **01**, 033, [arXiv:2006.09274 \[hep-ex\]](#).
- [54] A. M. Sirunyan *et al.* (CMS), *Measurements of $t\bar{t}$ differential cross sections in proton-proton collisions at $\sqrt{s} = 13$ TeV using events containing two leptons*, *JHEP* **02**, 149, [arXiv:1811.06625 \[hep-ex\]](#).
- [55] A. Tumasyan *et al.* (CMS), *Measurement of differential $t\bar{t}$ production cross sections in the full kinematic range using lepton+jets events from proton-proton collisions at $\sqrt{s} = 13$ TeV*, *Phys. Rev. D* **104**, 092013 (2021), [arXiv:2108.02803 \[hep-ex\]](#).
- [56] G. Aad *et al.* (ATLAS), *Measurements of top-quark pair differential and double-differential cross-sections in the ℓ +jets channel with pp collisions at $\sqrt{s} = 13$ TeV using the ATLAS detector*, *Eur. Phys. J. C* **79**, 1028 (2019), [Erratum: *Eur.Phys.J.C* 80, 1092 (2020)], [arXiv:1908.07305 \[hep-ex\]](#).
- [57] S. I. Alekhin and A. L. Kataev, *The nlo DGLAP extraction of $\alpha(s)$ and higher twist terms from ccf r $xf(3)$ and $f(2)$ structure functions data for neutrino n dis*, *Phys. Lett. B* **452**, 402–408 (1999), [arXiv:hep-ph/9812348](#).
- [58] A. L. Kataev, G. Parente, and A. V. Sidorov, *Higher twists and $\alpha(s)(M(Z))$ extractions from the NNLO QCD analysis of the CCFR data for the $xF(3)$ structure function*, *Nucl. Phys. B* **573**, 405–433 (2000), [arXiv:hep-ph/9905310](#).
- [59] A. L. Kataev, G. Parente, and A. V. Sidorov, *Improved fits to the $xF3$ CCFR data at the next-to-next-to-leading order and beyond*, *Phys. Part. Nucl.* **34**, 20–46 (2003), [Erratum: *Phys.Part.Nucl.* 38, 827–827 (2007)], [arXiv:hep-ph/0106221](#).
- [60] A. L. Kataev, *Neutrino deep inelastic scattering: New experimental and theoretical results*, *Frascati Phys. Ser.* **22**, 205–221 (2001), [arXiv:hep-ph/0107247](#).
- [61] W. Seligman, Ph.D. thesis, Columbia U. (1997).
- [62] U.-K. Yang *et al.* (CCFR/NuTeV), *A Measurement of $R = \sigma_L / \sigma_T$ in deep inelastic neutrino - nucleon scattering at the Tevatron*, *J. Phys. G* **22**, 775–780 (1996), [arXiv:hep-ex/9605005](#).
- [63] J. Pumplin, D. R. Stump, J. Huston, H. L. Lai, P. M. Nadolsky, and W.-K. Tung, *New generation of parton distributions with uncertainties from global QCD analysis*, *JHEP* **07**, 012, [arXiv:hep-ph/0201195 \[hep-ph\]](#).
- [64] S. Bailey and L. Harland-Lang, (2019), [arXiv:1909.10541 \[hep-ph\]](#).
- [65] J. Gao, M. Guzzi, and P. M. Nadolsky, *Charm quark mass dependence in a global QCD analysis*, *Eur. Phys. J. C* **73**, 2541 (2013), [arXiv:1304.3494 \[hep-ph\]](#).
- [66] R. D. Ball *et al.*, *Parton Distribution Benchmarking with LHC Data*, *JHEP* **04**, 125, [arXiv:1211.5142 \[hep-ph\]](#).
- [67] R. D. Ball, L. Del Debbio, S. Forte, A. Guffanti, J. I. Latorre, J. Rojo, and M. Ubiali (NNPDF), *Fitting Parton*

- Distribution Data with Multiplicative Normalization Uncertainties*, *JHEP* **05**, 075, [arXiv:0912.2276 \[hep-ph\]](#).
- [68] J. Gao, M. Guzzi, J. Huston, H.-L. Lai, Z. Li, P. Nadolsky, J. Pumplin, D. Stump, and C. P. Yuan, *CT10 next-to-next-to-leading order global analysis of QCD*, *Phys. Rev.* **D89**, 033009 (2014), [arXiv:1302.6246 \[hep-ph\]](#).
- [69] S. Forte and Z. Kassabov, *Why α_s cannot be determined from hadronic processes without simultaneously determining the parton distributions*, *Eur. Phys. J. C* **80**, 182 (2020), [arXiv:2001.04986 \[hep-ph\]](#).
- [70] S. Forte, J. Rojo, and R. Stegeman, in *2025 European Physical Society Conference on High Energy Physics* (2025) [arXiv:2511.22561 \[hep-ph\]](#).
- [71] P. Bevington and D. K. Robinson, *Data Reduction and Error Analysis for the Physical Sciences* (McGraw-Hill Education, 2002).
- [72] S. Navas *et al.* (Particle Data Group), *Review of particle physics*, *Phys. Rev. D* **110**, 030001 (2024).
- [73] P. Jimenez-Delgado and E. Reya, *Delineating parton distributions and the strong coupling*, *Phys. Rev. D* **89**, 074049 (2014), [arXiv:1403.1852 \[hep-ph\]](#).
- [74] S. Alekhin, J. Blümlein, and S. Moch, *NLO PDFs from the ABMP16 fit*, *Eur. Phys. J. C* **78**, 477 (2018), [arXiv:1803.07537 \[hep-ph\]](#).
- [75] I. Abt *et al.* (H1, ZEUS), *Impact of jet-production data on the next-to-next-to-leading-order determination of HERAPDF2.0 parton distributions*, *Eur. Phys. J. C* **82**, 243 (2022), [arXiv:2112.01120 \[hep-ex\]](#).
- [76] G. D'Agostini, *On the use of the covariance matrix to fit correlated data*, *Nucl. Instrum. Meth. A* **346**, 306–311 (1994).
- [77] G. D'Agostini, *Bayesian reasoning in high-energy physics: Principles and applications* (1999).
- [78] J. Pumplin, D. Stump, R. Brock, D. Casey, J. Huston, J. Kalk, H.-L. Lai, and W.-K. Tung, *Uncertainties of predictions from parton distribution functions. 2. The Hessian method*, *Phys. Rev.* **D65**, 014013 (2001), [arXiv:hep-ph/0101032 \[hep-ph\]](#).
- [79] A. D. Martin, W. J. Stirling, R. S. Thorne, and G. Watt, *Parton distributions for the LHC*, *Eur. Phys. J.* **C63**, 189–285 (2009), [arXiv:0901.0002 \[hep-ph\]](#).
- [80] R. A. Fisher, *Statistical methods for research workers* (Oliver and Boyd, Edinburgh, 1925) Chap. 4, an Internet version of the 1st edition at <http://psychclassics.yorku.ca/Fisher/Methods/>.
- [81] T. Lewis, *A simple improved-accuracy normal approximation for χ^2* , *Australian Journal of Statistics* **30A**, 160–168 (1988).
- [82] M. H. Quenouille, *Problems in plane sampling*, *Ann. Math. Statist.* **20**, 355 (1949).
- [83] J. W. Tukey, *Bias and confidence in not quite large samples (abstract)*, *The Annals of Mathematical Statistics* **29**, 614 (1958).
- [84] R. G. Miller, *The jackknife—a review*, *Biometrika* **61**, 1–15 (1974).
- [85] J. Erler and R. Ferro-Hernández, *Alternative to the application of PDG scale factors*, *Eur. Phys. J. C* **80**, 541 (2020), [arXiv:2004.01219 \[physics.data-an\]](#).
- [86] M. Yan, T.-J. Hou, Z. Li, K. Mohan, and C. P. Yuan, *Generalized statistical model for fits to parton distributions*, *Phys. Rev. D* **112**, 034008 (2025), [arXiv:2406.01664 \[hep-ph\]](#).
- [87] H. Akaike, *A new look at the statistical model identification*, *IEEE Transactions on Automatic Control* **19**,

716–723 (1974).

- [88] G. Schwarz, *Estimating the Dimension of a Model*, [The Annals of Statistics](#) **6**, 461 – 464 (1978).
- [89] S. Dulat, T.-J. Hou, J. Gao, M. Guzzi, J. Huston, P. Nadolsky, J. Pumplin, C. Schmidt, D. Stump, and C.-P. Yuan, *New parton distribution functions from a global analysis of quantum chromodynamics*, [Phys. Rev.](#) **D93**, 033006 (2016), [arXiv:1506.07443 \[hep-ph\]](#).